

Open Research Online

The Open University's repository of research publications and other research outputs

Study of the Effect of Mold Corner Shape on the Initial Solidification Behavior of Molten Steel Using Mold Simulator

Journal Item

How to cite:

Lyu, Peisheng; Wang, Wanlin; Long, Xukai; Zhang, Kaixuan; Gao, Erzhuo and Qin, Rongshan (2018). Study of the Effect of Mold Corner Shape on the Initial Solidification Behavior of Molten Steel Using Mold Simulator. Metallurgical and Materials Transactions B, 49(1) pp. 78–88.

For guidance on citations see [FAQs](#).

© 2017 The Minerals, Metals Materials Society and ASM International



<https://creativecommons.org/licenses/by-nc-nd/4.0/>

Version: Accepted Manuscript

Link(s) to article on publisher's website:

<http://dx.doi.org/doi:10.1007/s11663-017-1154-y>

Copyright and Moral Rights for the articles on this site are retained by the individual authors and/or other copyright owners. For more information on Open Research Online's data [policy](#) on reuse of materials please consult the policies page.

oro.open.ac.uk

Effect of Mold Corner Shape on the Initial Solidification Behavior of Molten Steel by Using Mold Simulator

Peisheng Lyu^{1,2}, Wanlin Wang^{1*,2}, Xukai Long¹, Kaixuan Zhang¹, Erzhuo Gao¹, Rongshan Qin³

1. School of Metallurgy and Environment, Central South University, Changsha, Hunan, 410083, China.

2. National Center for International Research of Clean Metallurgy, Central South University, Changsha, Hunan, 410083, China

3. The department of Engineering and Innovation, The Open University, Milton Keynes, MK7 6AA, UK

Corresponding Author: Wanlin Wang. E-mail: wanlin.wang@gmail.com

Abstract:

The chamfered mold with a typical corner shape (angle between the chamfered face and hot face is 45 degree) was applied to the mold simulator study in this paper, and the results were compared with the previous results from a well-developed right-angle mold simulator system. The results suggested that the designed chamfered structure would increase the thermal resistance and weaken the two-dimensional heat transfer around the mold corner, causing the homogeneity of the mold surface temperatures and heat fluxes. In addition, the chamfered structure can decrease the fluctuation of the steel level and the liquid slag flow around the meniscus at mold corner. The cooling intensities at different longitudinal sections of shell are close to each other due to the similar time-average solidification factors, which are $2.392 \text{ mm/s}^{1/2}$ (section A-A: chamfered center), $2.372 \text{ mm/s}^{1/2}$ (section B-B: 135° corner) and $2.380 \text{ mm/s}^{1/2}$ (section D-D: face), respectively. For the same oscillation mark (OM), the heights of OM roots at different positions (profile L1(face), profile L2(135° corner) and profile L3(chamfered center)) are very close to each other. The average value of height difference (H_D) between two OM roots for L1 and L2 is 0.22 mm, and for L2 and L3 is 0.38 mm. Finally, with the help of metallographic examination, the shapes of different hooks were also discussed.

1. INTRODUCTION

Surface defects, such as longitudinal or transverse cracks, longitudinal off-corner depressions, and deep oscillation marks (OMs), have widely existed in the continuous casting strands.^[1] Many surfaces defects originate from the initial solidification of molten steel inside the mold.^[2,3] If the surface defects could not be removed by scarfing or

grinding prior to the rolling process, some detrimental defects such as slivers and blisters would occur on the final rolled products.^[4-7] Therefore, the elimination of surface defects is crucial for improving the quality of final continuous casting products.

Many works related to the meniscus phenomena (such as heat transfer, fluid flow and interaction of forces), which affect the initial solidification and the formation of OM_s, have been done to understand the formation mechanism of surface defects.^[8,9] Tomono^[10] and Ackerman^[11] proposed the overflowing and folding mechanism for the formation of OM_s through the observations on the scaled caster by using organic compounds and steel. Based on the industrial measurements and observations combined with the mathematical modeling, Thomas et al.^[12] proposed a detailed mechanism for the formation of hooks and their associated OM_s. Lopez et al.^[13] built a mathematical model for the metal-slag flow coupled with the heat transfer and solidification to study the influence of slag infiltration on the shell solidification and the formation of the OM_s. Brimacombe et al.^[1,14] conducted the study to elucidate the relation between the mold hot-face temperatures at the meniscus, slag thickness, and the OM depth. Matsushita et al.^[15] have directly observed the meniscus of molten steel in the mold through a quartz glass window mounted in the mold wall, to investigate the relationship between the surface wave motion of molten steel and the mold oscillation. Furthermore, the dip-type mold simulator was also applied to study the meniscus phenomena by many researchers,^[16-20] and their results showed that the dip-type mold simulator could provide an ideal way for the study of initial solidification behaviors of the molten steel. Wang et al. have conducted the detailed study on the complex interrelationship between the solidified shell surface profile, heat flux, shell thickness, mold level fluctuation, and the infiltrated slag

film by using the mold simulator system.^[21] The works regarding the effect of the mold oscillation and mold level fluctuation on the initial solidification behaviors have also been investigated by Wang et al.^[22]

Many industrial practices to minimize strand surface defects have been developed, including the non-sinusoidal oscillation,^[23-25] low density and exothermic mold slag,^[26] hot top mold,^[27] and the adjustment of the composition of liquid steel, etc. In addition, the methods to optimize the copper mold structure, such as mold coating, mold taper, inner cavity shape and configuration of cooling channels, have been proposed. Based on the results from industrial trials and mathematical models, Brimacombe et al.^[14] suggested a good slab quality would be expected, through achieving the objectives of having a similar two-broad faces behavior, in which the mold hot-face temperature at the meniscus could be controlled by changing the copper-plate thickness, cooling-channel configuration and mold coatings. Park et al.^[28] built a thermal-elastic-plastic-creep finite element model to investigate the influence of the mold corner radius on the thermo-mechanical behavior and longitudinal crack formation in billet casting. Besides, Samarasekera et al.^[29] designed a new mold taper with the aim to minimize the shell-mold interaction or binding to improve the quality of cast product. Shen et al.^[30] and Hu et al.^[31] studied the effect of the mold corner shape and taper on the temperature and stress distribution in the solidified slab through mathematical simulations, and then proposed a suitable mold corner shape and taper for slab casting. According to the results of electrical analogue and mathematical model in conjunction with plant trials, Patrick et al. suggested that the mold copper end plates with a 40 mm chamfer can reduce the transverse corner cracking of slabs^[32]. However, the research regarding the effect of the mold corner shape on the

initial solidification behaviors around the meniscus region during the continuous casting process, which is of great importance for the optimization of mold corner shape and the control of surface quality, has barely been reported.

In this paper, a chamfered mold with a typical corner shape (angle between the chamfered face and hot face is 45 degree) was applied to the mold simulator tests. Then, with the help of the 2D-inverse heat conduction problem (IHCP)^[33], power spectral density (PSD) and fast Fourier transformation (FFT) analysis, the mold surface temperatures and heat fluxes across the mold surface during the casting process were calculated, and their fluctuations at different positions of the mold were also discussed. Next, the solidification factors and surface profiles of the shell were analyzed. Finally, the results in this study were compared with our previous results from a well-developed right-angle mold simulator system,^[34] to understand the effect of the mold corner shape on the initial solidification behaviors of molten steel around the meniscus region.

II. EXPERIMENTAL APPARATUS AND PROCESS

As shown in Figure 1, the chamfered mold simulator system applied to this study is constructed based on the previous well-developed right-angle mold simulator system,^[34] and the only difference between above is the corner shape of the mold. The experimental configuration and process in this study are similar to the previous system and have already been described in details^[34]. Except for the corner shape, the size and water-cooling channels for this chamfered one are designed as same as the right-angle mold, which are shown in Figure 2, where q_f and q_c represent the heat fluxes across the mold hot face and chamfer. The in-mold wall temperatures during a mold simulator run are measured by the high-speed data acquisition system (including NI data acquisition

card and 16 highly sensitive thermocouples). The acquisition speed is chosen as 60 times per second based on the Shannon sampling theorem^[35]. As shown in Figure 2 and Figure 3, the distribution principle of thermocouples inside the chamfered mold is as same as the right-angle mold^[34]. Then the measured in-mold temperatures are delivered to the **2D-IHCP** mathematical model^[33] to recover the heat fluxes and temperatures on the mold surface.

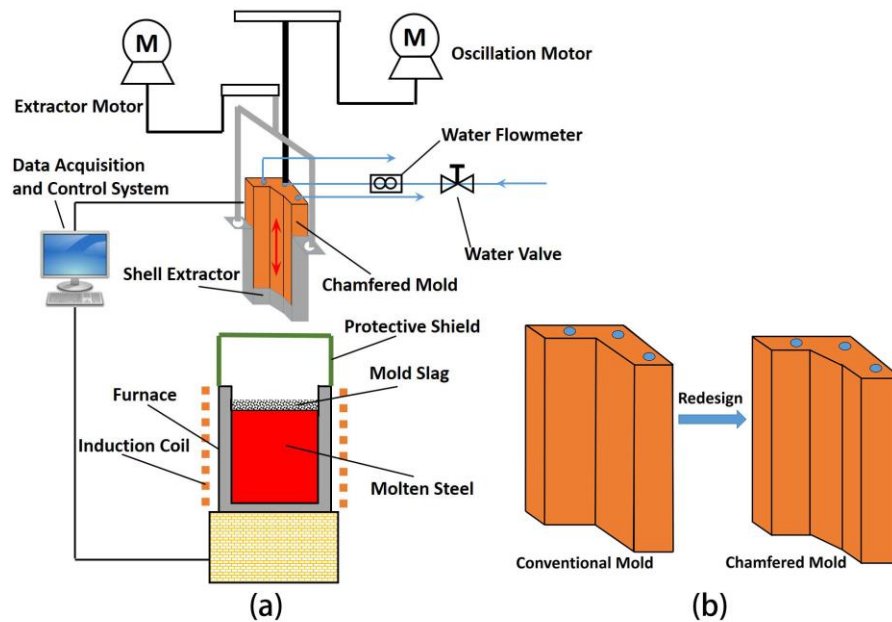


Fig. 1—Schematic of the chamfered mold simulator system: (a) chamfered mold simulator system and (b) redesign of the chamfered copper mold.

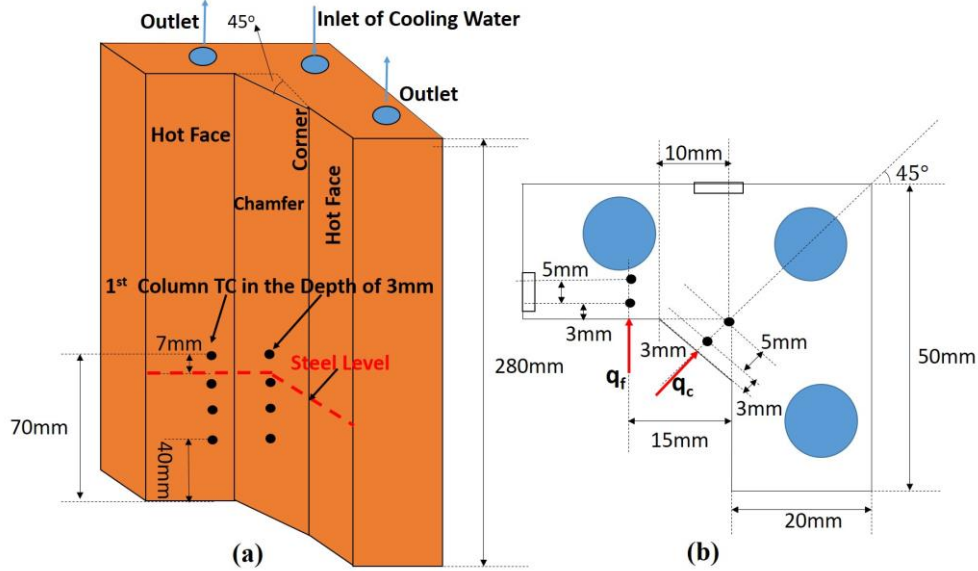


Fig. 2—The size of the chamfered mold: (a) schematic of the chamfered mold and (b) cross section of the mold.

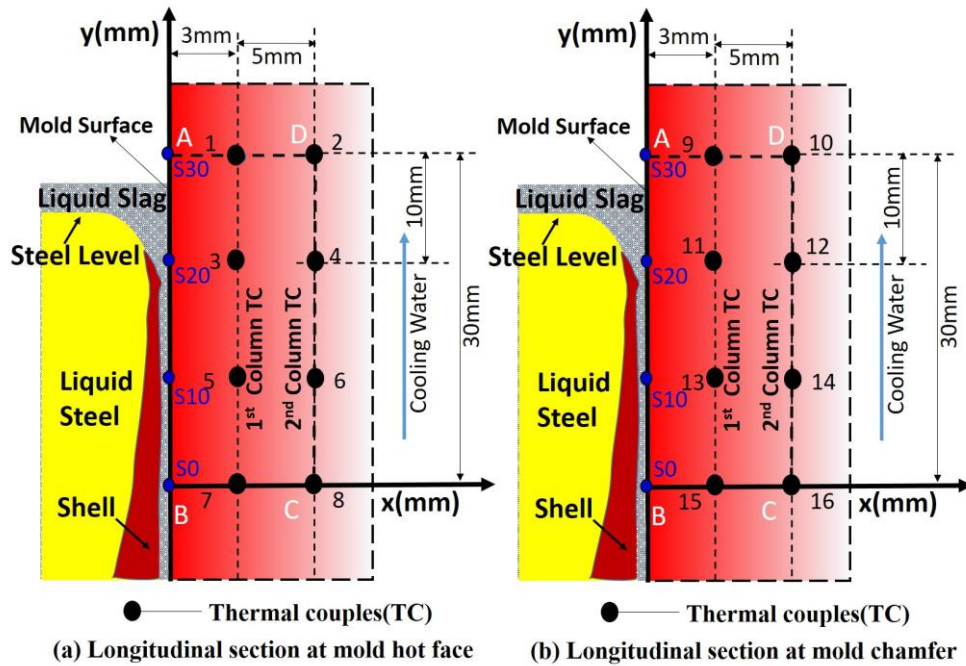


Fig. 3—Locations of the thermocouples at the mold longitudinal section: (a) longitudinal section at the mold hot face and (b) longitudinal section at the mold chamfer.

The tests have been repeated three times, and the measured in-mold temperatures by

the embedded thermocouples are similar to each other. One typical example is shown in

Figure 4. The steel grade, mold slag composition and the casting conditions in the present experiments are as same as the right-angle mold simulator experiments^[34], and shown in Tables I, II, and III, respectively. It should be noted that the melt temperature of the liquid steel is measured at first and then the mold simulator system is started, and the measurement error is within ± 2 K (± 2 °C) (by Tungsten-Rhenium thermocouple). Additionally, the duration of the cast (corresponding to the stage III in Figure 4) is 5.5 seconds during a mold simulator run, and the casting length of shell is about 55 mm. In Figure 3, rectangle ABCD is the computational domain of 2D-IHCP mathematical model^[33], where AB is the mold surface that close to the hot shell and CD is another side that close to the cooling channel. S0~S30 correspond to the locations of points on the mold surface; S represents surface and the number represents the value of y-coordinate (mm). As shown in Figure 3, the steel level is located at S23 during the cast period, and the shell tip is located around S20 when the shell is lifted out of molten steel bath. The thickness of molten slag layer above steel bath during the continuous casting period is about 7 mm. The positions of steel level and shell tip with respect to the mold surface in the present study are identical to those in the right-angle mold simulator tests.

III. RESULTS AND DISCUSSION

A. Measured Temperatures and Calculated Mold Surface Temperatures

The measured in-mold temperatures by the 16 thermocouples during a mold simulator run are shown in Figure 4, where the stage III corresponds to the continuous casting process (from 60.8s to 66.3s). Figure 5 shows the mold surface temperatures at the mold hot face and chamfer, which are calculated by the developed 2D-IHCP mathematical model^[33]. It can be observed that the mold surface temperatures at the mold

chamfer (Figure 5(b)) are very close to those at the mold hot face (Figure 5(a)). For example, the time-average surface temperatures at S20 (around the meniscus) for the mold chamfer and hot face during continuous casting in stage III are 363.1 K (90.1 °C) and 364.1 K (91.1 °C), respectively. For the right-angle mold simulator tests in our previous work^[34], the surface temperatures at the mold corner are lower than those at the mold hot face, due to the two-dimensional heat transfer at horizontal plane around the mold corner, and the time-average surface temperatures at S20 for the mold corner and hot face during continuous casting are 363.6 K (90.6 °C) and 368.2 K (95.2 °C), respectively^[34]. In other words, the homogeneity of temperatures distribution in the chamfered mold is better than that in the right-angle mold. This is because the chamfered structure increases the thermal resistance between the shell and water-cooling channel, and weakens the two-dimensional heat transfer around the mold corner. During the stage III, the fluctuation amplitudes of the mold surface temperatures at S20 for the mold chamfer and hot face are about 2.4 K (2.4 °C) and 3.3K (3.3 °C), respectively. But in the case of right-angle mold simulator, the fluctuation amplitudes at S20 are about 4.5 K (4.5 °C) and 2.9 K (2.9 °C) for the mold corner and hot face, respectively. So, it can be found that the chamfered structure does inhibit the fluctuation amplitude of the mold corner surface temperatures, causing the similarity of the surface temperatures between the mold chamfer and hot face.

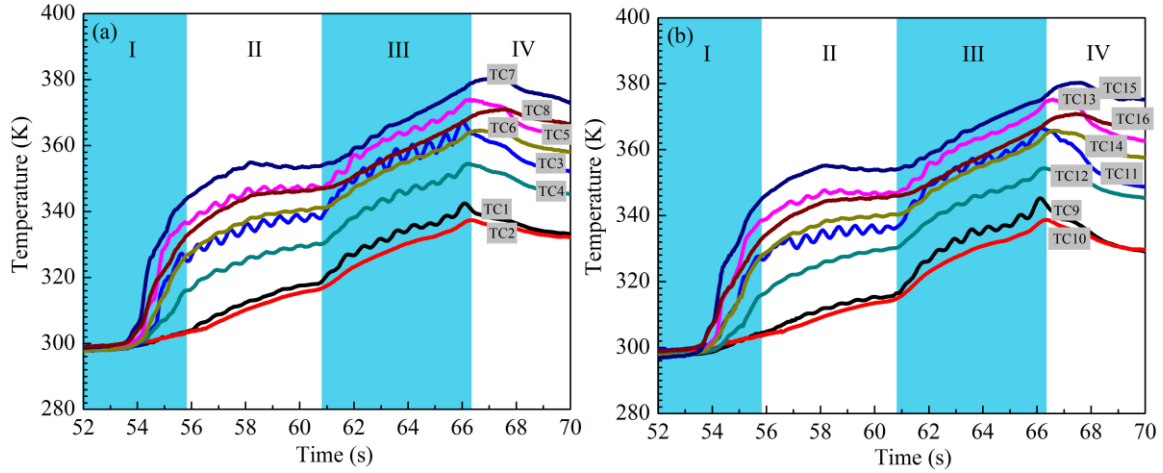


Fig. 4—The measured in-mold temperatures during a mold simulator run: (a) measured temperatures at the mold hot face and (b) measured temperatures at the mold chamfer.

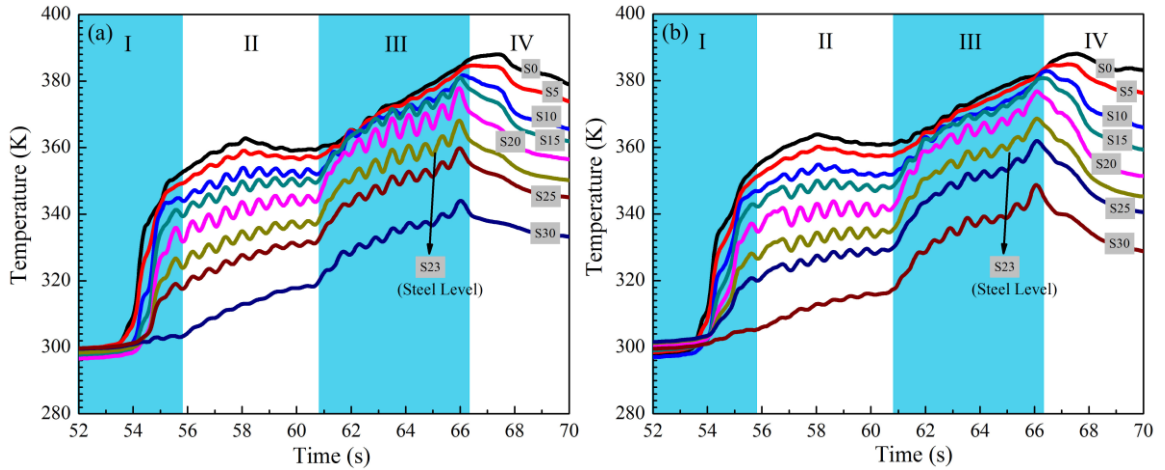


Fig. 5—Temperatures at the mold surface calculated by the **2D-IHCP** model: (a) mold surface temperatures at the mold hot face and (b) mold surface temperatures at the mold chamfer.

B. Variation of the Heat Fluxes across Mold Surface, PSD Analysis and FFT Analysis

During the continuous casting process, the heat fluxes across the mold hot face and chamfer are also calculated through the **2D-IHCP** model, and shown in Figures 6(a) and 7(a), respectively. It is clear that the general heat fluxes across the mold chamfer are very close to those across the mold hot face. For example, the time-average heat flux at S20 for the mold chamfer during continuous casting is 1.29 WM/m^2 with the maximum value of 1.81 MW/m^2 , and it is 1.36 WM/m^2 with the maximum value of 1.75 MW/m^2 for the

mold hot face. But for the case of right-angle mold simulator^[34], as the heat dissipation
 around the mold corner is two-dimensional, the general heat fluxes at the mold corner are
 higher, where the time-average heat flux at S20 is 1.60 WM/m² with the maximum value
 of 2.16 MW/m². The existence of the chamfered structure inside the mold increases the
 total thermal resistance around the corner and weakens the two-dimensional heat transfer,
 and thus decreases the heat fluxes around the mold chamfer, to achieve the
 homogenization of the general heat fluxes between the mold chamfer and hot face, which
 is consistent with the results reported by Patrick that the heat fluxes are appropriately
 uniform around the corner region in the case of larger chamfered mold during the plant
 trials^[32]. Then the PSD analysis^{[36][37]} is applied to the heat fluxes across both the mold
 hot face and chamfer, and the results are shown in Figures 6(b) and 7(b). It can be
 observed that the signals of 1.67 Hz in both cases are much stronger than other signals,
 and they are identical to the mold oscillation frequency. In addition, the low-frequency
 heat flux signals (< 0.8 Hz) can also be observed in Figures 6(b) and 7(b), which are
 related to the low-frequency phenomena around the meniscus region, such as air gap
 formation, unevenness solidification, and fluctuation of steel level.

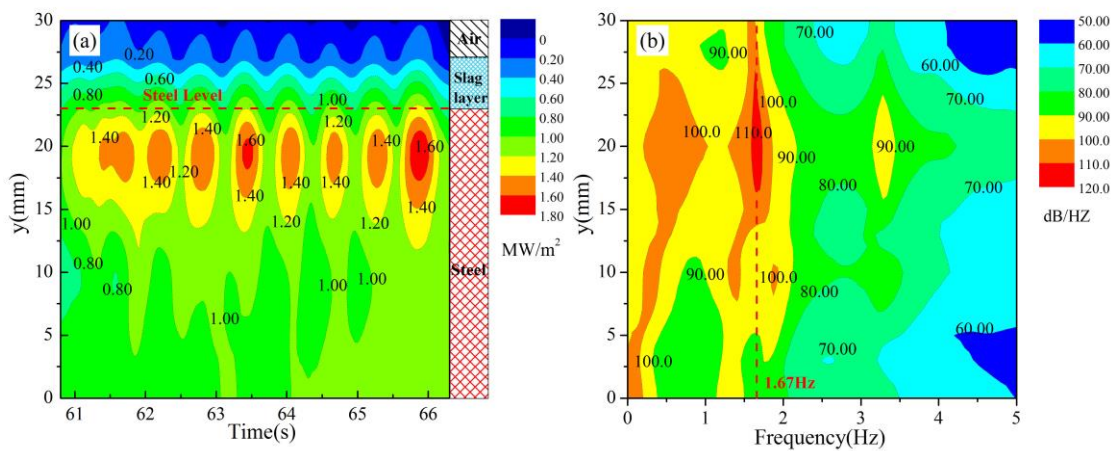


Fig. 6—The heat fluxes across mold surface at the mold hot face and their **PSD** analysis during the continuous casting period: (a) the heat fluxes contour map and (b) the **PSD** contour map.

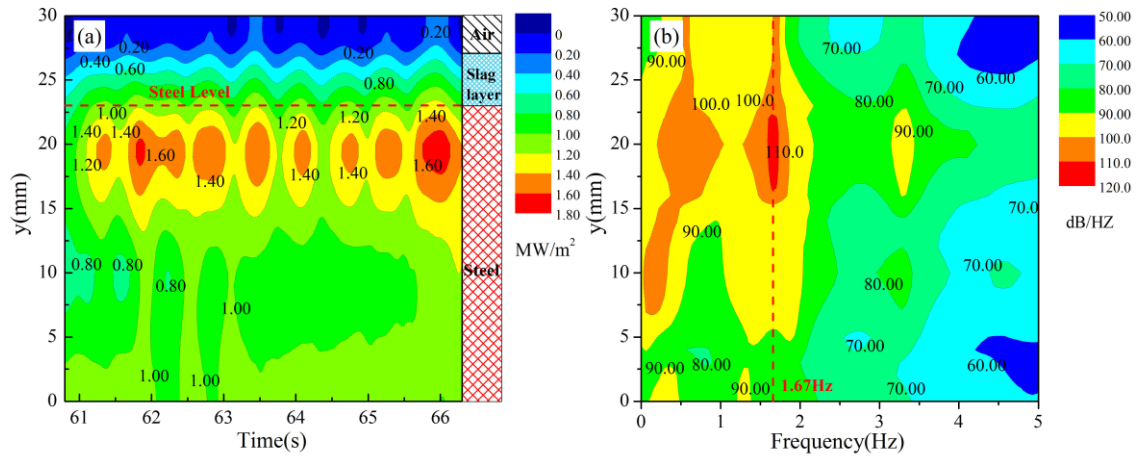


Fig.7—The heat fluxes across mold surface at the mold chamfer and their **PSD** analysis during the continuous casting period: (a) the heat fluxes contour map and (b) the **PSD** contour map.

The **PSD** analysis results of the heat fluxes at S20 for both cases are shown in Figures 8. Apparently, there are four characteristic signals with the frequency of f_1 , f_2 , f_3 , and f_4 , respectively, appearing in the figure. Signal f_1 is related to the low-frequency phenomena, and signals f_2 , f_3 , and f_4 are related to the high-frequency phenomena. For all characteristic heat flux signals, the intensity of signals for the mold chamfer is close to the mold hot face. However, for the case of right-angle mold simulator tests, the intensity of signals for the mold corner is higher than that for the mold hot face, because of the unsteadiness of the melt flow around the meniscus in mold corner. So, it may be concluded that the chamfered structure of copper mold decreases the fluctuation of steel level and liquid slag flow in the meniscus area. The heat fluxes at S20 are spilt into low- and high-frequency components through the **FFT** filter^[36,37] with the delineation frequency of 0.8 Hz, and shown in Figure 9 (a). The low-frequency heat fluxes at S20 for the mold chamfer and hot face reach relatively steady state with the fluctuation around

the baselines of 1.44 WM/m² and 1.38 WM/m², respectively, while the largest fluctuation amplitudes of the high-frequency heat fluxes for the mold chamfer and hot face are 0.26 WM/m² and 0.34 WM/m², respectively. But for the case of right-angle mold simulator tests^[34], the low-frequency heat fluxes at S20 for the mold corner and hot face reach relatively steady state around the baselines of 1.67 WM/m² and 1.31 WM/m², respectively, while the largest fluctuation amplitudes of the high-frequency heat fluxes for mold corner and hot face are 0.46 WM/m² and 0.31 WM/m², respectively, as shown in Figure 9 (b). It suggests that the baselines of the low-frequency heat fluxes or the fluctuation amplitudes of the high-frequency heat fluxes for the mold chamfer and hot face are closer to each other, which is due to the designed chamfered structure around the corner that shows the capability to homogenize the fluctuation of steel level and liquid slag flow around the mold corner.

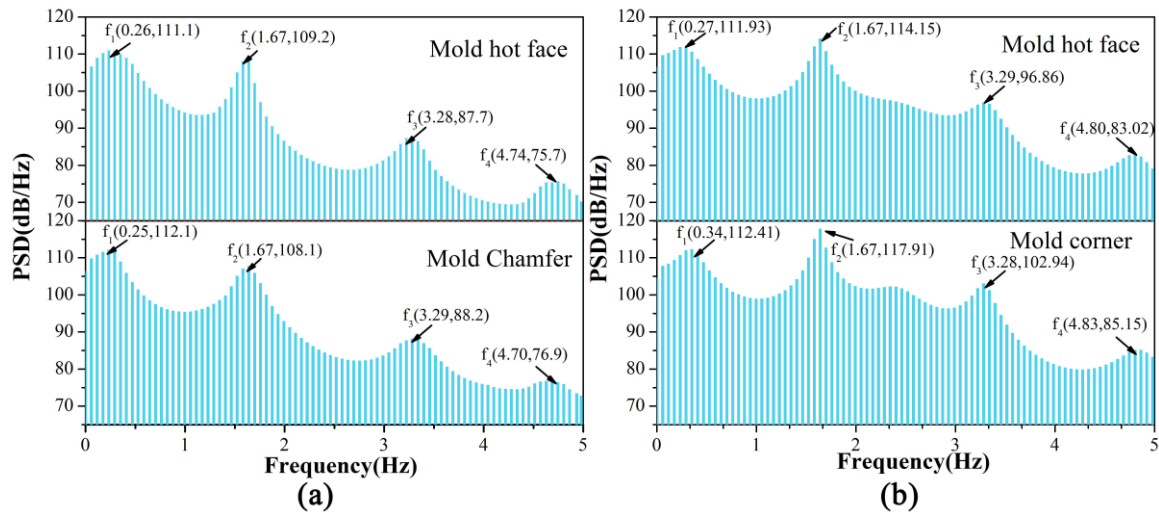


Fig.8—The **PSD** analysis of the heat fluxes at S20 during the continuous casting period: (a) **PSD** of the heat fluxes across mold surface for the chamfered mold simulator tests and (b) **PSD** of the heat fluxes across mold surface for the right-angle mold simulator tests^[33].

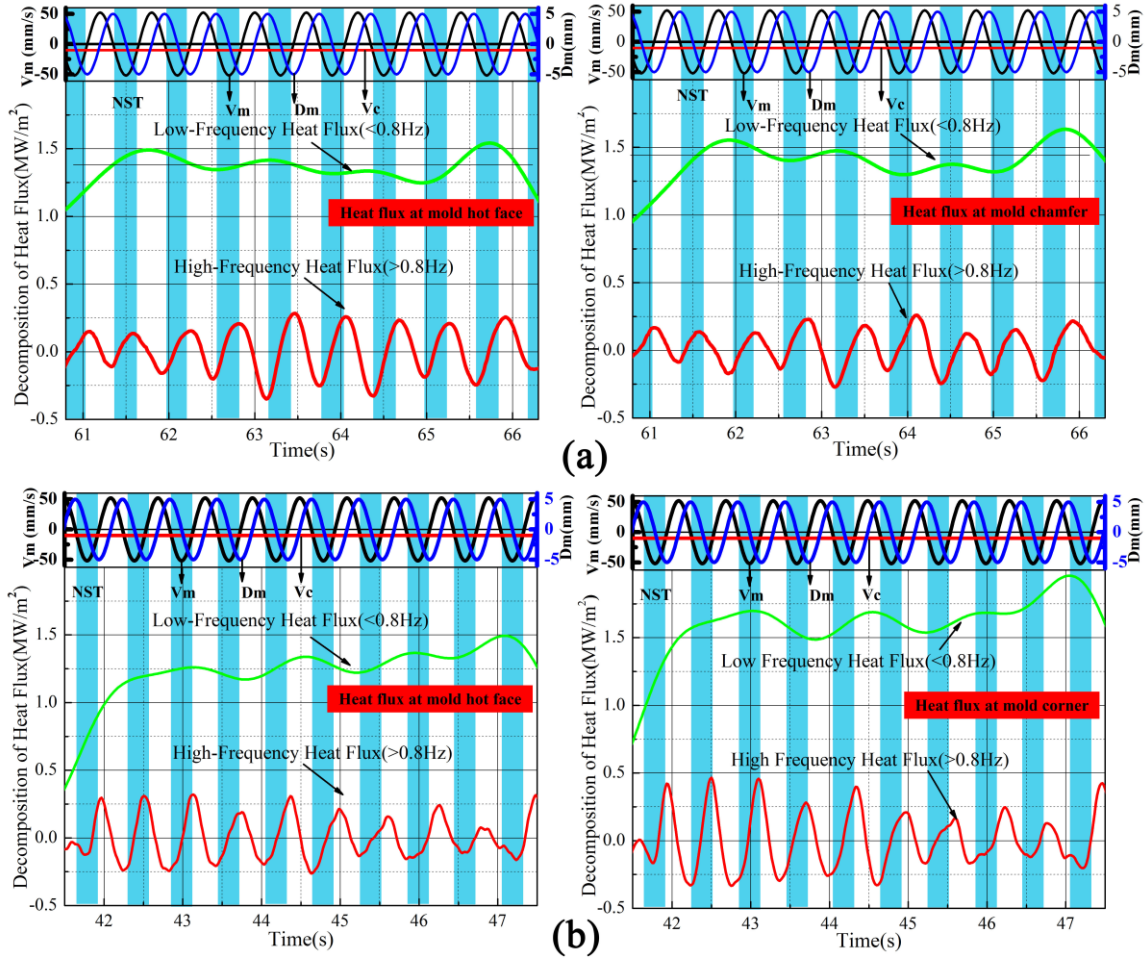
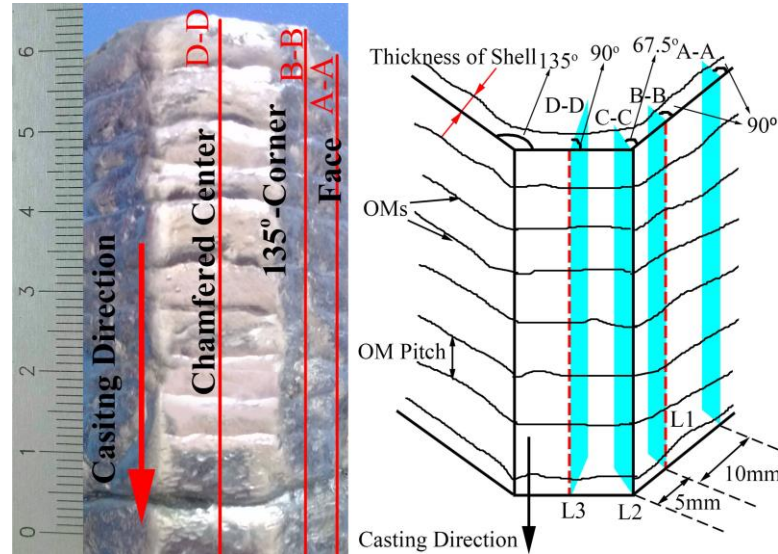


Fig. 9—The decomposition of the heat fluxes at S20 during the continuous casting period:
 (a) the heat fluxes across mold surface for the chamfered mold simulator tests and
 (b) the heat fluxes across mold surface for the right-angle mold simulator tests^[33].

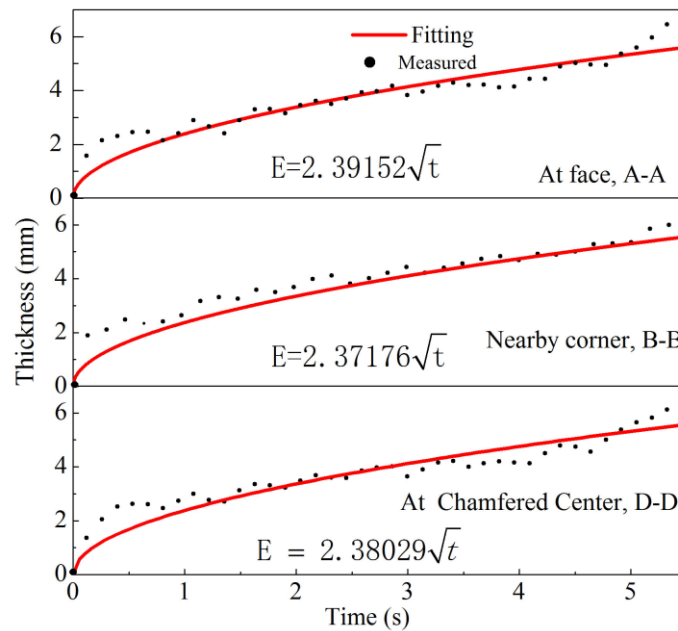
C. Thickness of Initial Solidified Shell and Thickness Fitting

Figure 10 shows the initial solidified shell obtained from this study, from which three longitudinal sections (section A-A, section B-B and section D-D) were cut. Then the thickness (E , mm) of the shell versus time t ($t = L/V_c$), where L (mm) is the length of shell and V_c (mm/s) is the casting speed at different sections, is fitted with the solidification square root law: $E = \bar{K}\sqrt{t}$ (where \bar{K} is the time-average solidification factor, $\text{mm/s}^{1/2}$), as shown in Figure 11. The time-average solidification factors are 2.392 $\text{mm/s}^{1/2}$ (A-A), 2.372 $\text{mm/s}^{1/2}$ (B-B) and 2.380 $\text{mm/s}^{1/2}$ (D-D), respectively, and it may

246 imply that the cooling intensities at different parts of the shell are close to each other due
 247 to the similar time-average solidification factors. For the right-angle mold simulator tests,
 248 the cooling intensity at the corner is stronger, and the corresponding solidification factor
 249 is $2.766 \text{ mm/s}^{1/2}$ that is higher than others. Therefore, it is confirmed again that the
 250 chamfered structure can improve the heat-transfer uniformity of the copper mold.



251 Fig. 10—The initial solidified shell: (a) the shell obtained from this study and (b) the
 252 schematic of the shell.
 253



254 Fig. 11—Thickness fitting of the shell at different positions.
 255

D. The Surface Profile of the Initial Solidified Shell and Its Metallographic Examination

The surface profiles (L1, L2 and L3) for different parts of the shell shown in Figure 12 were measured by a contact profilometer, in which OM1~OM9 represent the OMs on the shell surface. It can be found that for the same OM, the heights of OM roots at different positions (L1, L2 and L3) are very close to each other, which differs from the case of right-angle mold simulator tests^[34]. The measured pitch, depth, and height difference (H_D) for each OM are listed in Table IV. The average OM pitches for profile L1, L2 and L3 are 5.52 mm, 5.57 mm and 5.68 mm, respectively, which are slightly lower than the theoretical OM pitch, $T_{pitch} = one\ cycle\ time \times Vc = 0.6\ s \times 10\ mm/s = 6\ mm$. This difference may be caused by the fluctuation of casting speed or steel level. The average OM depths for profile L1, L2 and L3 are 0.44 mm, 0.45 mm and 0.45 mm, respectively, which are close to that for the case of right-angle mold simulator tests (0.42 mm at face and 0.46 mm at corner). Clearly, the most different profile character between the chamfered shell and the right-angle shell is the H_D between two OM roots for the same OMs. The average value of H_D between two OMs roots for L1 and L2 is 0.22 mm, and for L2 and L3 is 0.38 mm. But for the case of right-angle shell, the maximum value of H_D between two roots (at corner and face) for the same OMs is 2.88 mm, the minimum value is 0.49 mm and the average value is 1.65 mm. The reason could be explained as the deeper penetration of the overflowing molten steel occurred around the shell corner due to the formed larger corner gap^[34]. As discussed above, the cooling intensities of the chamfered mold at different positions are close to each other, which causes the similar solidification shrinkage. Therefore, the gap sizes between the shell and

mold wall at different positions (such as the chamfered center, 135° corner and hot face) are expected to be similar. Consequently, the penetration of the overflowing molten steel between the shell and mold wall is similar; thus the value of H_D is very small.

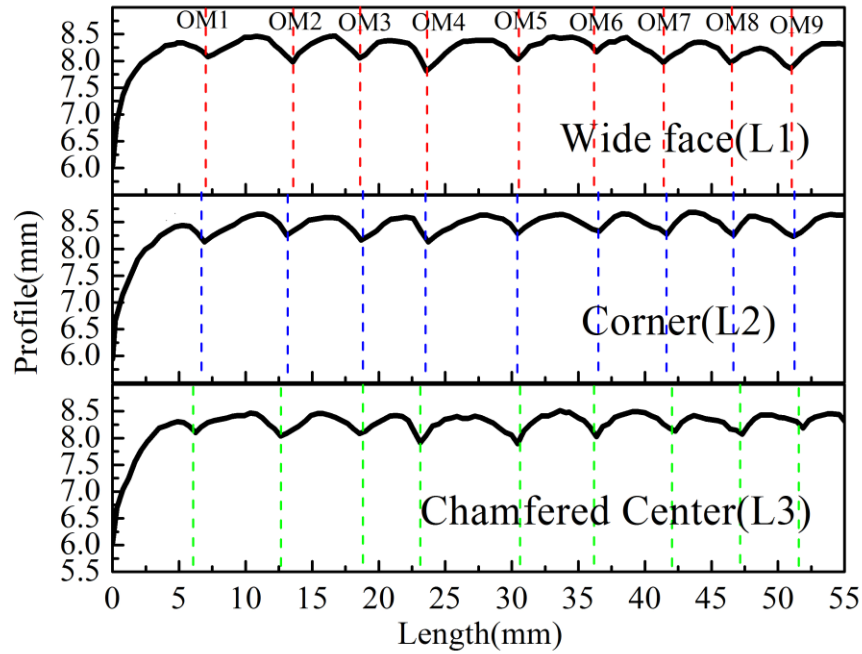


Fig.12—The measured profile of shell surface at different positions
Metallographic examinations of the shells have been conducted for the observations

of the sub-surface microstructure in the vicinity of **OMs**. In the present study, **OM4** and **OM8** are chosen as the representatives for the metallographic examinations, where the formation of **OM8** is prior to **OM4**. Figure 13 shows the metallographs of different sections (**A-A**, **B-B**, **C-C** and **D-D**) for **OM4** and **OM8**, where the hook shape and overflow region can be observed. For the same **OM**, the hook shapes are similar to each other at different positions of the shell. This may be attributed to the similar phenomena occurred at different positions (**A-A**, **B-B**, **C-C** and **D-D**) around the meniscus, i.e. (i) cooling ability (ii) steel level fluctuation and (iii) pressure from liquid slag channel^[38] or pressure from slag rim^[39]. As shown in Figure 13, it is found that the hook length and

hook-bending angle of **OM4** is larger than those of **OM8**. As suggested by Thomas et al.^[40] that hooks are initiated by the meniscus solidification; hence, during the formation of **OM4**, the longer hook length for **OM4** may be due to the lower superheat around the meniscus region, and correspondingly more meniscus solidification. Besides, in a mold simulator run, the thickness of slag rim attached to the mold surface increases gradually because of the consecutive cooling by the water-cooling mold. According to the report that the **OMs** are produced by the interaction between the slag rim and the solidified meniscus,^[14,41] a thicker slag rim during the negative strip time of the formation of **OM4** would result in a more intensive interaction between the slag rim and the solidified meniscus. Consequently, the bending angle of the hook for **OM4** is larger than that for **OM8**.

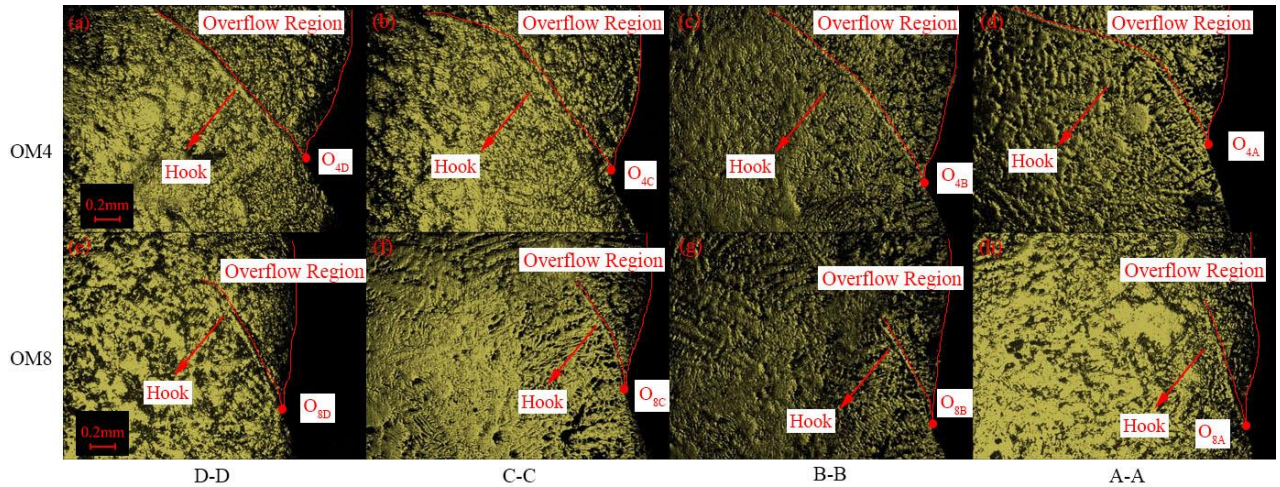


Fig. 13—Metallographs of the shell around the **OMs**: (a) ~ (d) metallographs of shell around the **OM4** at different longitudinal sections and (e) ~ (h) metallographs of shell around the **OM8** at different longitudinal sections.

IV. CONCLUSIONS

The chamfered mold simulator system has been used in this paper to study the initial solidification behaviors of the molten steel around the meniscus inside the chamfered

mold. Also, the study results were compared with our previous results from a well-developed right-angle mold simulator system, to understand the effect of mold corner shape on the initial solidification behaviors of molten steel. The main conclusions are summarized as follows:

1. For the chamfered mold simulator tests, the mold surface temperatures and general heat fluxes at the mold chamfer are very close to those at the mold hot face. In contrast, for the case of the right-angle mold simulator tests, the mold surface temperatures around the corner are lower than those at the mold hot face, and general heat fluxes at the mold corner are larger than those at the mold hot face. This is because the chamfered structure increases the thermal resistance and weakens the two-dimensional heat transfer around the mold corner.

2. The four characteristic signals f_1 , f_2 , f_3 , and f_4 can be observed from the **PSD** analysis results of the heat fluxes at S20, where the intensities of these signals are close to each other. The similarity of the fluctuation amplitudes of the surface temperatures and heat fluxes for both mold chamfer and hot face suggests that the chamfered structure can decrease the fluctuation of the steel level and liquid slag flow around the meniscus at mold corner.

3. The thickness of solidified shell (longitudinal section near the corner, at the mold hot face and at the chamfered center) and solidification time accord with the solidification square root law. The cooling intensities at different parts of the chamfered shell are close to each other due to the similar time-average solidification factors, which are 2.392 mm/s^{1/2} (section **A-A**: chamfered center), 2.372 mm/s^{1/2} (section **B-B**: 135° corner) and 2.380 mm/s^{1/2} (section **D-D**: face), respectively, indicating that the chamfered structure

can improve the heat-transfer uniformity of the copper mold.

4. The gap size formed between the shell and mold wall is expected to be similar due to the similar cooling intensity of the chamfered mold at different positions, which allows the similar penetration of the overflowing molten steel between the shell and mold wall. So, it can be found, for the same **OM**, the heights of **OM** roots at different positions (profile **L1**(face), profile **L2**(135° corner) and profile **L3**(chamfered center)) are very close to each other. The average value of **H_D** between two **OMs** roots for **L1** and **L2** is 0.22 mm, and for **L2** and **L3** is 0.38 mm.

5. The similar hook shape is caused by the similar phenomena occurred around the meniscus, such as cooling ability of chamfered mold, steel level fluctuation, pressure from liquid slag channel and slag rim. A longer hook length may be due to the larger volume meniscus solidification, and a thicker slag rim during the negative strip time would introduce a larger bending angle of the hook.

ACKNOWLEDGEMENTS

The financial support from National Science Foundation of China (51661130154, U1760202) and Newton Advanced Fellowship (NA150320) is greatly acknowledged.

REFERENCES

- [1] R.B. Mahapatra, J.K. Brimacombe, I.V. Samarasekara, N. Walker, E.A. Paterson, and J.D. Young: Metall. Mater. Trans. B, 1991, vol. 22B, pp. 861-74.
- [2] M.M. Wolf: Continuous Casting, vol. 9, Initial Solidification and Strand Surface Quality of Peritectic Steels, Iron and Steel Society, Warrendale, PA, 1997, pp. 1–111.
- [3] B.H. Nakato, M. Ozawa, K. Kinoshita, Y. Habu, and T. Emi: Trans. Iron Steel Inst. Jpn., 1984, vol. 24 (11), pp. 957–65.
- [4] K.D. Schmidt, F. Friedel, K.P. Imlau, W. Jäger, and K.T. Müller: Steel Res. Int., 2003, Vol. 74(11), pp. 659-666.
- [5] S. Harada, S. Tanaka, H. Misumi, S. Mizoguchi, and J. Horiguchi: Iron Steel Inst. Jpn. Int., 1990, vol. 30 (4), pp. 310–16.

- [6] S. Mazumdra and S.K. Ray: *Sadhana*, 2001, vol. 26 (1–2), pp. 179–98.
- [7] K. Schwerdfeger and H. Sha: *Metall. Mater. Trans. B*, 2000, vol. 31B, pp. 813–26.
- [8] M.M. Wolf: *Process. Technol.*, 1995, vol. 13, pp. 99–117.
- [9] M.M. Wolf: *Steel Times Int.*, 1992, vol. 16 (2), p. 37.
- [10] H. Tomono: Ph.D. Dissertation: Swiss Federal Institute of Technology, Lausanne, Switzerland, 1979.
- [11] P. Ackermann: Ph.D. Dissertation: Swiss Federal Institute of Technology, Lausanne, Switzerland, 1983.
- [12] J. Sengupta, B. G. Thomas, H. J. Shin, G. G. Lee and S. H. Kim: *Metall. Mater. Trans. A*, 2006, vol. 37(5), pp. 1597–611.
- [13] P.E.R. Lopez, K.C. Mills, P.D. Lee, and B. Santillana: *Metall. Mater. Trans. B*, 2012, vol. 43B (1), pp. 109–22.
- [14] R.B. Mahapatra, J.K. Brimacombe, I.V. Samarasekera: *Metall. Mater. Trans. B*, 1991, vol. 22(B), pp. 875–88.
- [15] A. Matsushita, K. Isogami, M. Temma, T. Ninomiya, and K. Tsutsumi: *Trans. Iron Steel Inst. Jpn.*, 1988, vol. 28 (7), pp. 531–34.
- [16] Badri, T.T. Natarajan, C.C. Snyder, K.D. Powers, F.J. Mannion, and A.W. Cramb: *Metall. Mater. Trans. B*, 2005, vol. 36B (3), pp. 355–71.
- [17] Badri, T.T. Natarajan, C.C. Snyder, K.D. Powers, F.J. Mannion, M. Byrne, and A.W. Cramb: *Metall. Mater. Trans. B*, 2005, vol. 36B (3), pp. 373–83.
- [18] J. Park, E. Ko, J. Choi, and I. Sohn: *Met. Mater. Int.*, 2014, vol. 20 (6), pp. 1103–14.
- [19] E. Ko, J. Choi, J. Park, and I. Sohn: *Met. Mater. Int.*, 2014, vol. 20 (1), pp. 141–51.
- [20] S.C. Moon: Ph.D. Dissertation, University of Wollongong, Wollongong, AUS, 2015.
- [21] H. Zhang, W. Wang, F. Ma, and L. Zhou: *Metall. Mater. Trans. B*, 2015, vol. 46B (5), pp. 2361–73.
- [22] H. Zhang and W. Wang: *Metall. Mater. Trans. B*, 2016, vol. 47B (2), pp. 920–31.
- [23] T. Araki and M. Ikeda: *Can. Metall. Q.*, 1999, vol. 38 (5), pp. 295–300.
- [24] M. Suzuki, H. Mizukami, T. Kitagawa, K. Kawakami, S. Uchida, and Y. Komatsu: *ISIJ Int.*, 2007, vol. 31 (3), pp. 254–61.
- [25] H. Shin, G. Lee, W. Choi, S. Kang, J. Park, S. Kim, and B. G. Tomas: *AISTech 2004 Iron and Steel Technology Conf. Proc.*, Nashville, TN, 2004, pp. 1157–70.
- [26] Genzano, J. Madias, D. Dalmaso, J. Petroni, D. Biurrun, and G.D. Gresia: *Iron Steelmaker*, 2002, vol. 29(6), pp. 23–26.
- [27] I.G. Saucedo: *Steelmaking Conf. Proc.*, ISS-AIME, Warrendale, PA, 1991, pp. 45–53.
- [28] J. K. Park, B. G. Thomas, and I.V. Samarasekera: *Ironmak. Steelmak.*, 2002, vol. 29(5), pp. 359–75.
- [29] Chow, I.V. Samarasekera, B.N. Walker, and G. Lockhart: *Ironmak. Steelmak.*, 2002, vol. 29(1), pp. 61–69.
- [30] Zhang, S. Lei, S. Zeng, and H. Shen: *ISIJ Int.*, 2014, vol. 54 (2), pp. 336–41.
- [31] P. Hu, H. Zhang, M. Wang, M. Zhu, X. Zhang, Y. Zhang, and Z. Zhang: *Metall. Res. Technol.*, 2015, vol. 112 (1), pp. 1–10.
- [32] B. Patrick, S.G. Thornton. ECSC report, no. 7210.CA/821 (C1.3/85), Luxembourg, 1990.
- [33] H. Zhang, W. Wang, and L. Zhou: *Metall. Mater. Trans. B*, 2015, vol. 46B, pp. 2137–52.
- [34] P. Lyu, W. Wang, and H. Zhang: *Metall. Mater. Trans. B*, 2017, vol. 46B (1), pp.

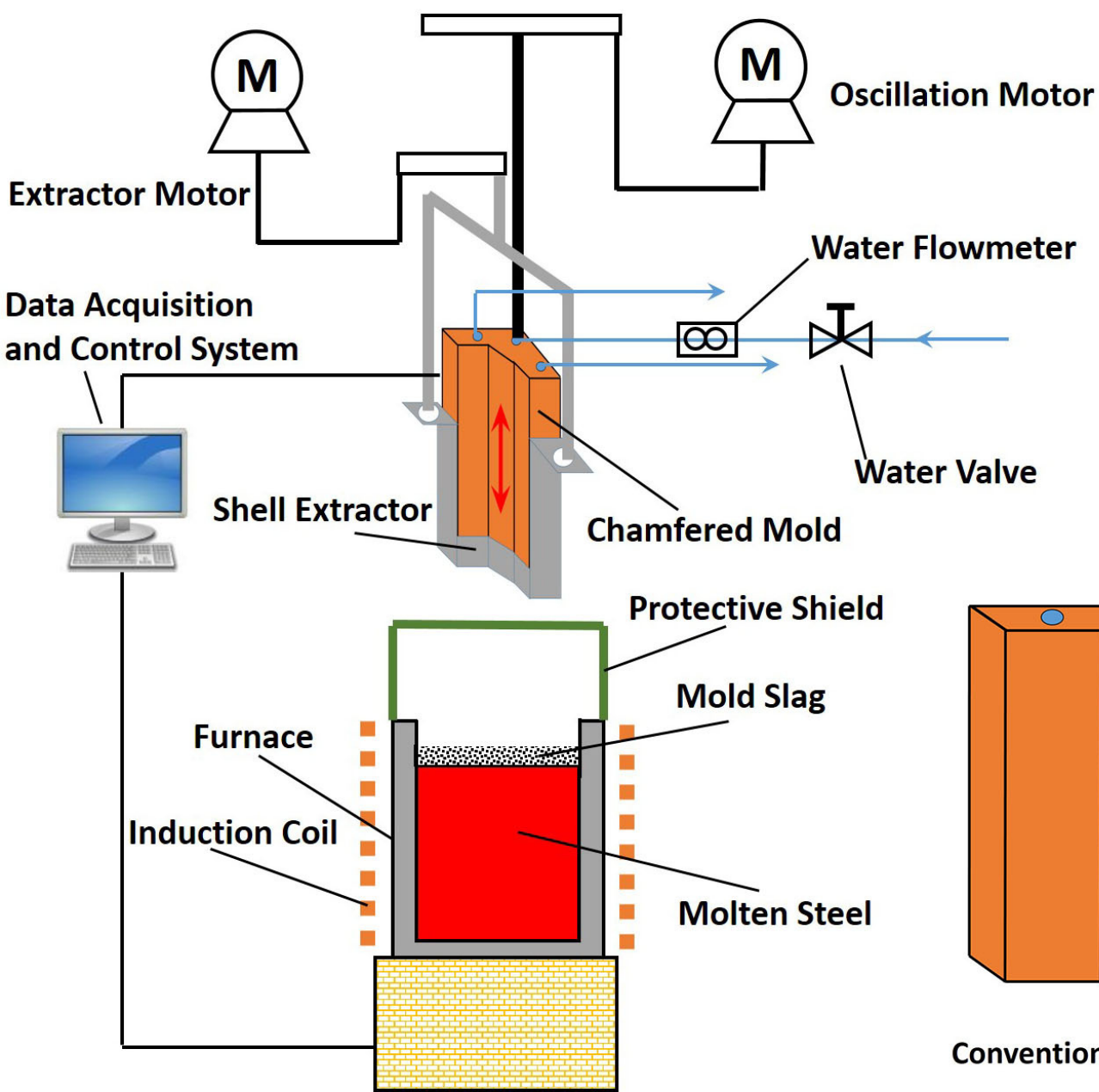
247–259

- [35] C.E. Shannon: Proc. IRE, 1949, vol. 37, pp. 10–21.
- [36] A.V. Oppenheim, R.W. Schaffer, and J.R. Buck: Discrete-Time Signal Processing, Prentice-Hall, Englewood Cliffs, 1989.
- [37] S.W. Smith: Digital Signal Processing: A Practical Guide for Engineers and Scientists, Newnes, Boston, 2003.
- [38] Takeuchi and J.K. Brimacombe: Metall. Mater. Trans. B, 1984, vol. 15B, pp. 493–509.
- [39] T. Emi, H. Nakato, Y. Iida, K. Emota, R. Tachibana, T. Imai, and H. Bada: Steelmaking Conf. Proc., Iron and Steel Society, Warrendale, PA, 1978, vol. 61, pp. 350–61.
- [40] J. Sengupta, H.J. Shin, B.G. Thomas, and S.H. Kim: Acta Mater., 2006, vol. 54 (4), pp. 1165–73.
- [41] H. Tomono, P. Ackermann, W. Kurz, and W. Heinemann: Solidification Technology in the Foundry and Casthouse, The Metals Society, Coventry, England, 1983, pp. 524–31.

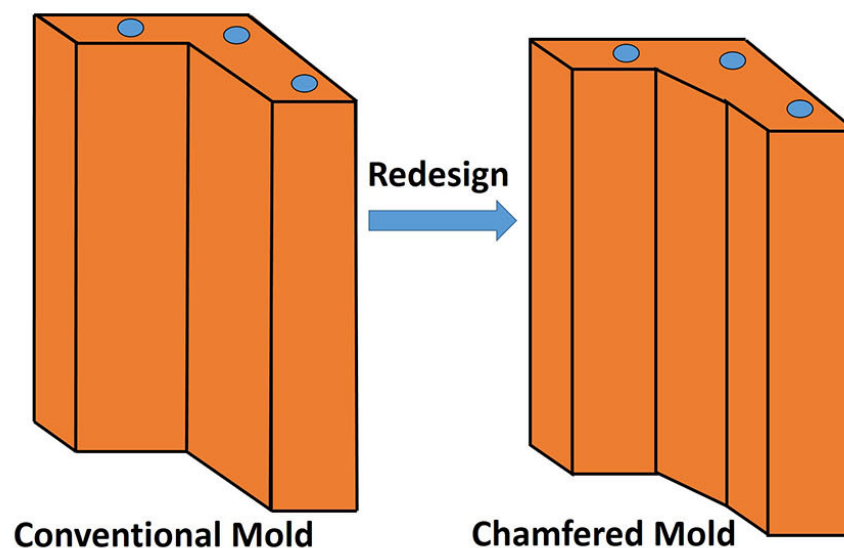
Figure List:

- Fig. 1—Schematic of the chamfered mold simulator system: (a) chamfered mold simulator system and (b) redesign of the chamfered copper mold.
- Fig. 2—The size of the chamfered mold: (a) schematic of the chamfered mold and (b) cross section of the mold.
- Fig. 3—Locations of the thermocouples at the mold longitudinal section: (a) longitudinal section at the mold hot face and (b) longitudinal section at the mold chamfer.
- Fig. 4—The measured in-mold temperatures during a mold simulator run: (a) measured temperatures at the mold hot face and (b) measured temperatures at the mold chamfer.
- Fig. 5—Temperatures on the mold surface calculated by 2D-IHCP model: (a) mold surface temperatures at the mold hot face and (b) mold surface temperatures at the mold chamfer.
- Fig. 6—The heat fluxes across mold surface at the mold hot face and their PSD analysis during the continuous casting period: (a) the heat fluxes contour map and (b) the PSD contour map.
- Fig. 7—The heat fluxes across mold surface at mold chamfer and their PSD analysis during the continuous casting period: (a) the heat fluxes contour map and (b) the PSD contour map.
- Fig. 8—The PSD analysis of the heat fluxes at S20 during the continuous casting period: (a) PSD of the heat fluxes across mold surface for chamfered mold simulator tests and (b) PSD of the heat fluxes across mold surface for right-angle mold simulator tests^[33].
- Fig. 9—The decomposition of the heat fluxes at S20 during the continuous casting period: (a) the heat fluxes across mold surface for the chamfered mold simulator tests and (b) the heat fluxes across mold surface for the right-angle mold simulator tests^[33].
- Fig. 10—The initial solidified shell: (a) the shell obtained from this study and (b) the schematic of the shell.

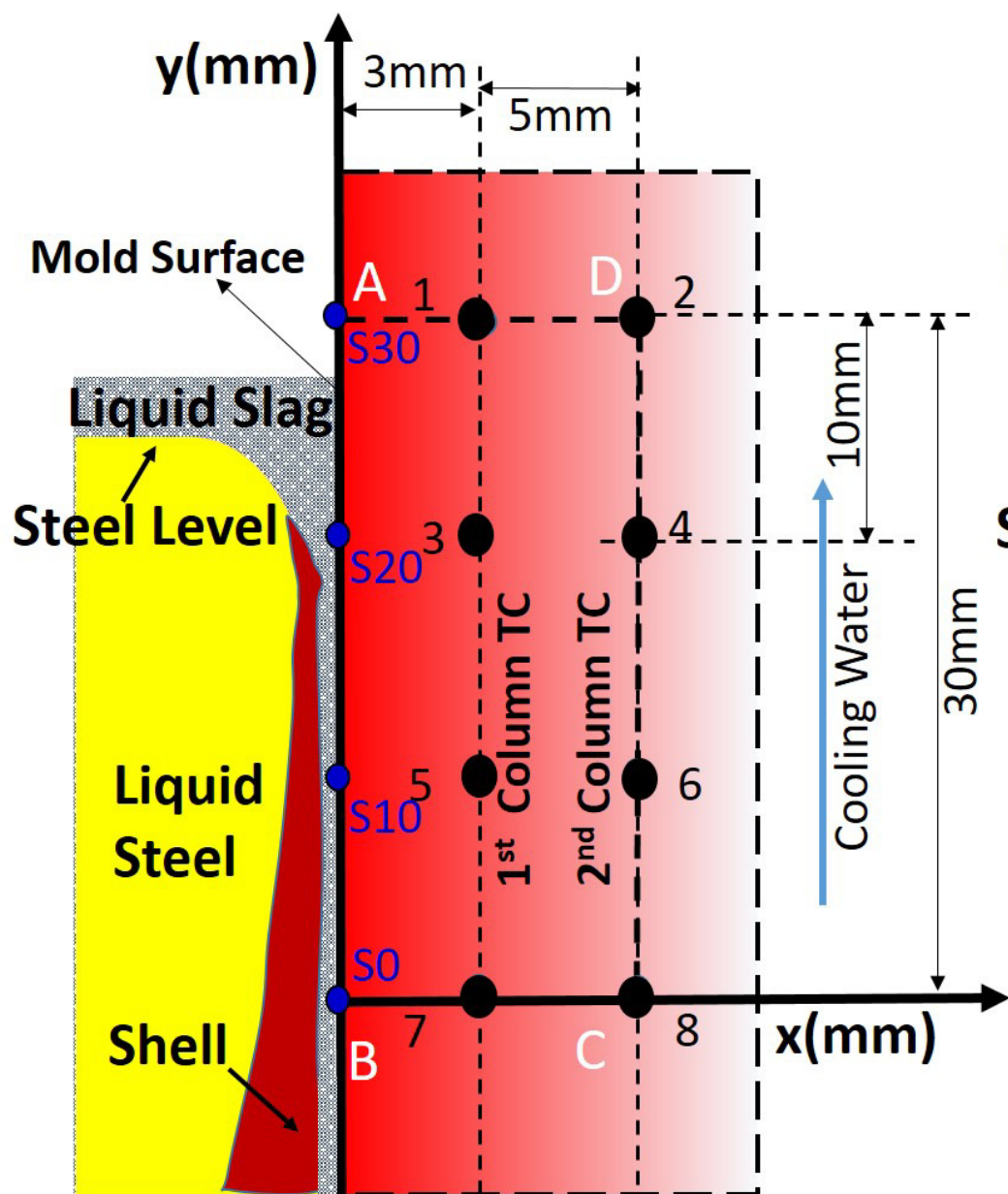
455 Fig. 11—Thickness fitting of the shell at different positions.
456 Fig. 12—The measured profile of shell surface at different positions.
457 Fig. 13—Metallographs of the shell around the **OMs**: (a) ~ (d) metallographs of shell
458 around the **OM4** at different longitudinal sections and (e) ~ (h) metallographs
459 of shell around the **OM8** at different longitudinal sections.



(a)

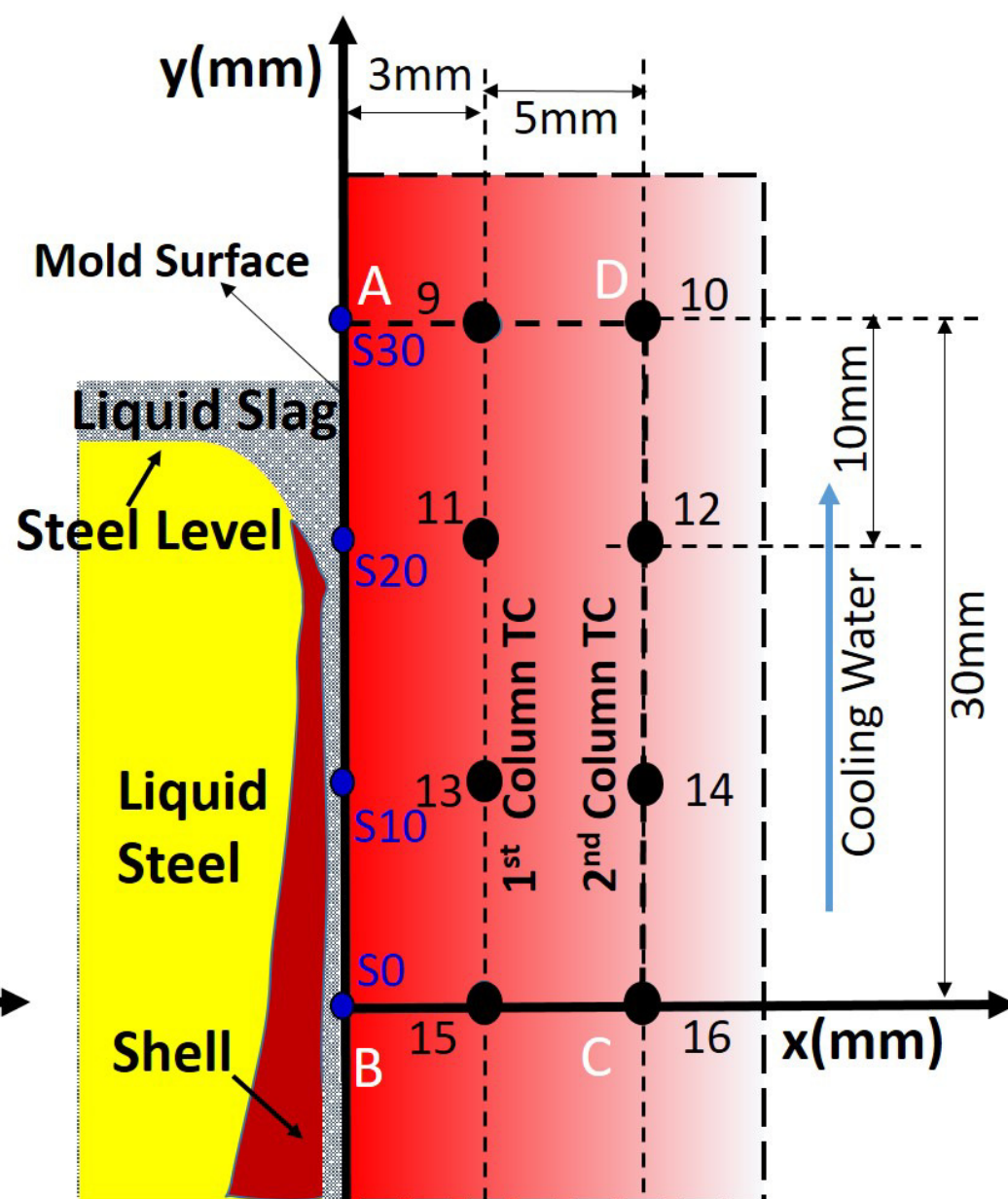


(b)



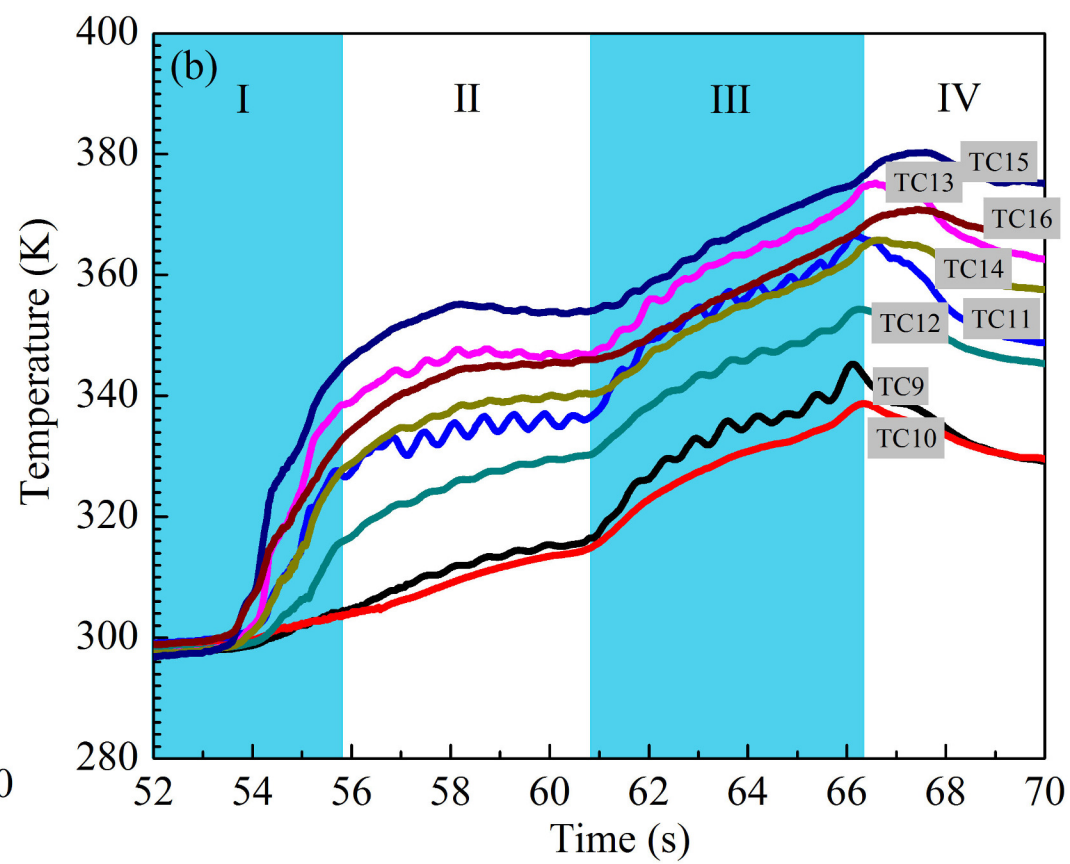
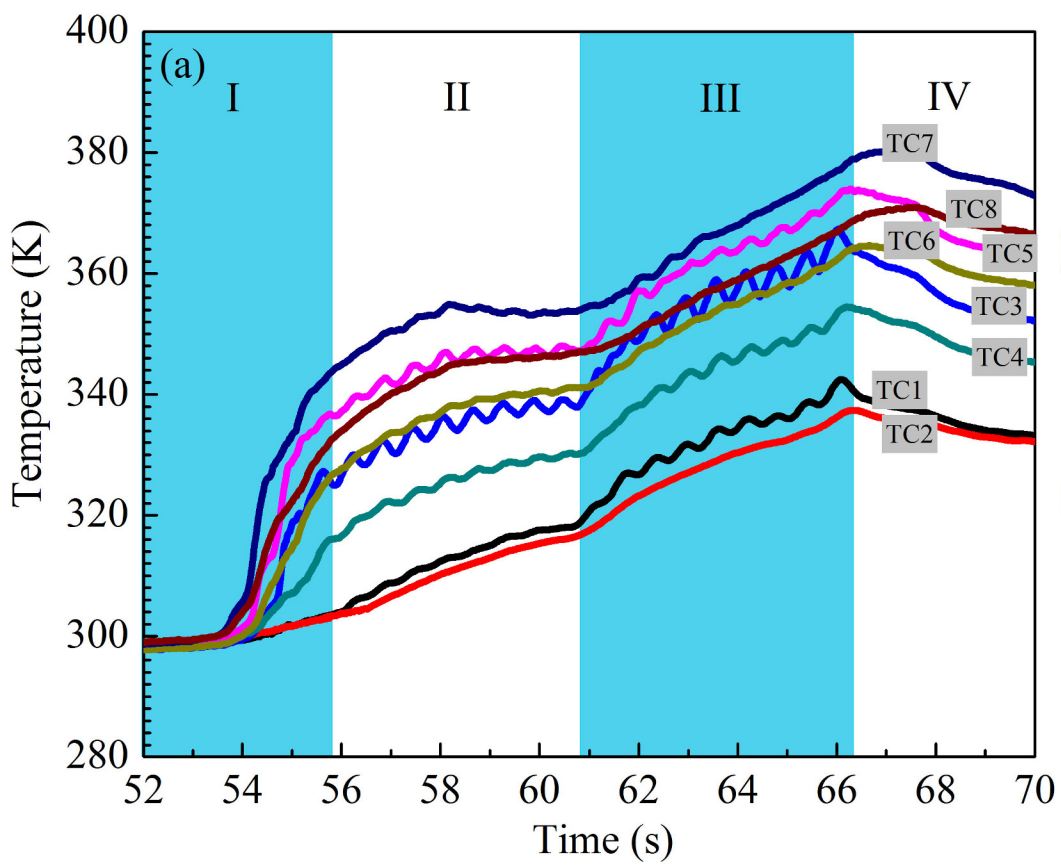
● Thermal couples(TC)

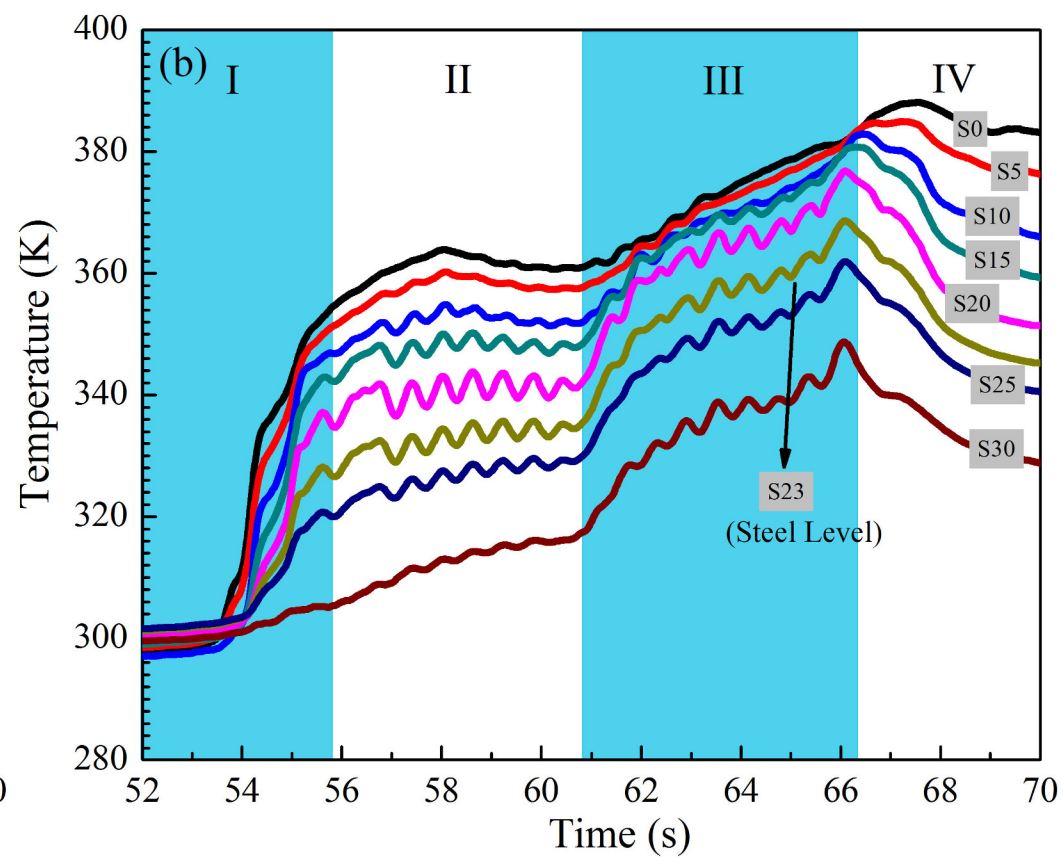
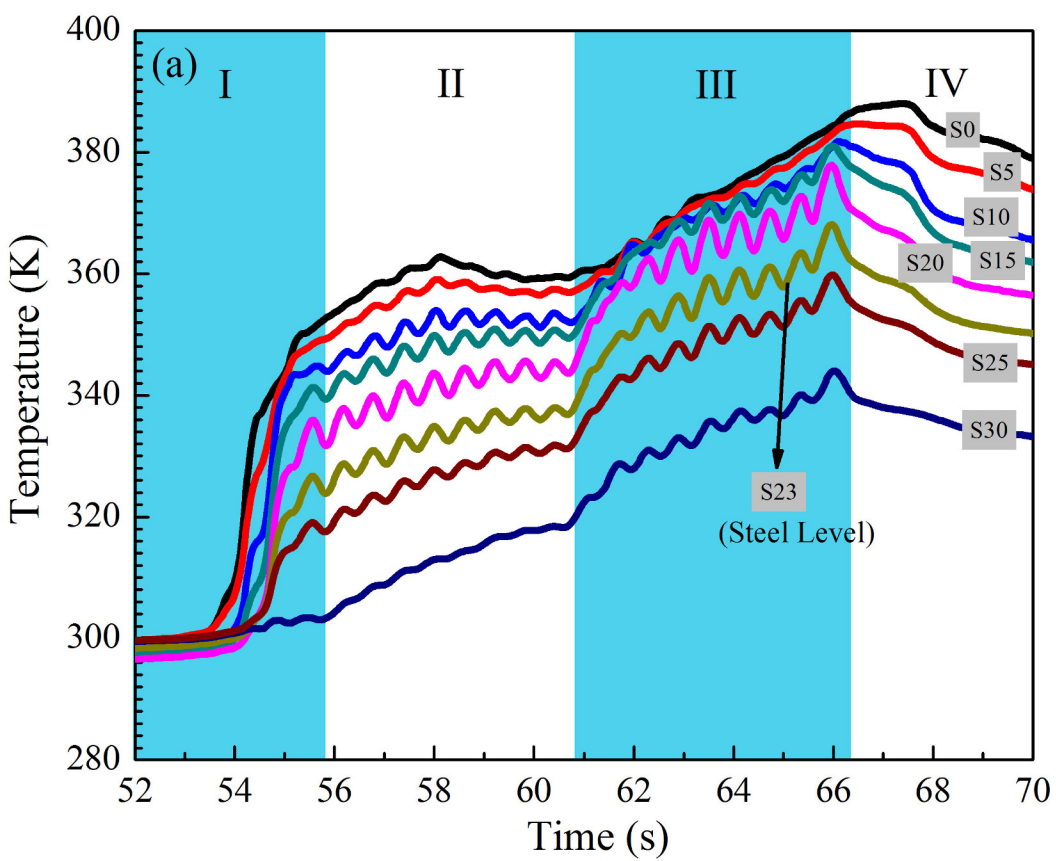
(a) Longitudinal section at mold hot face

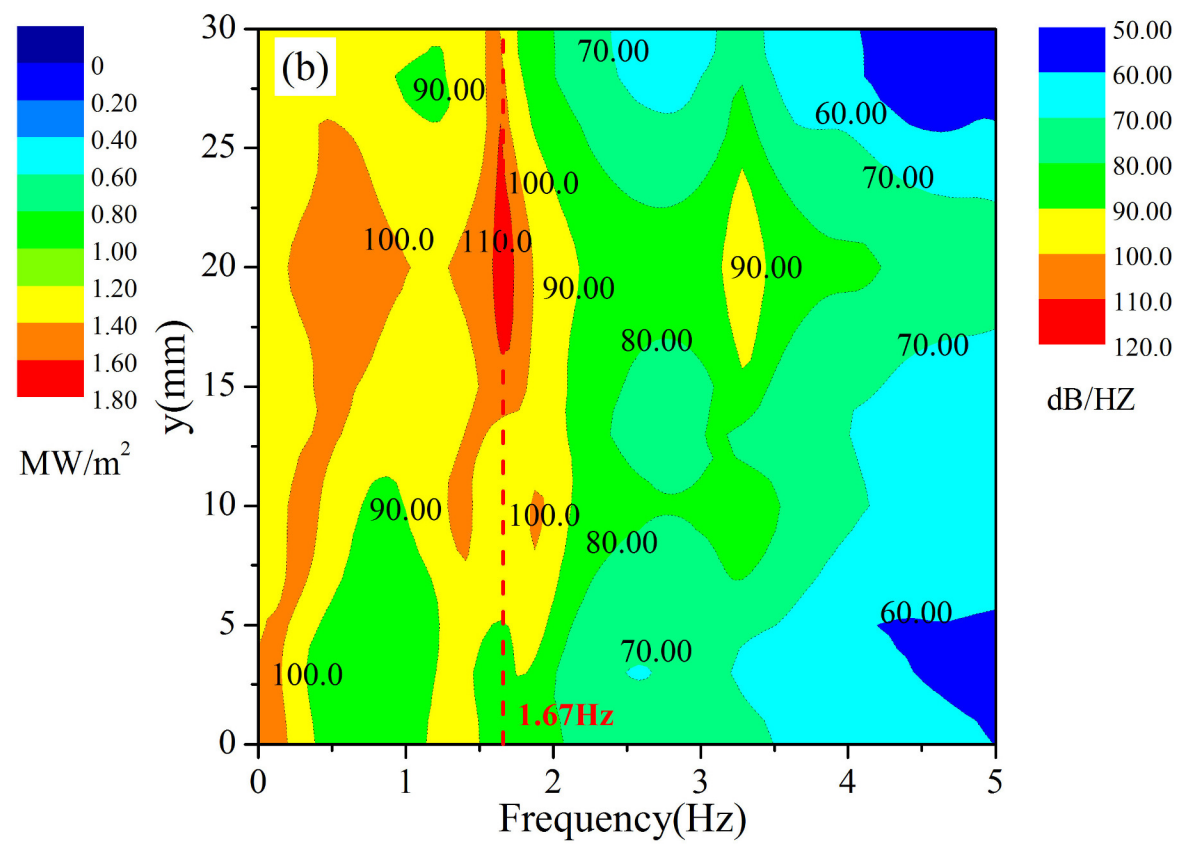
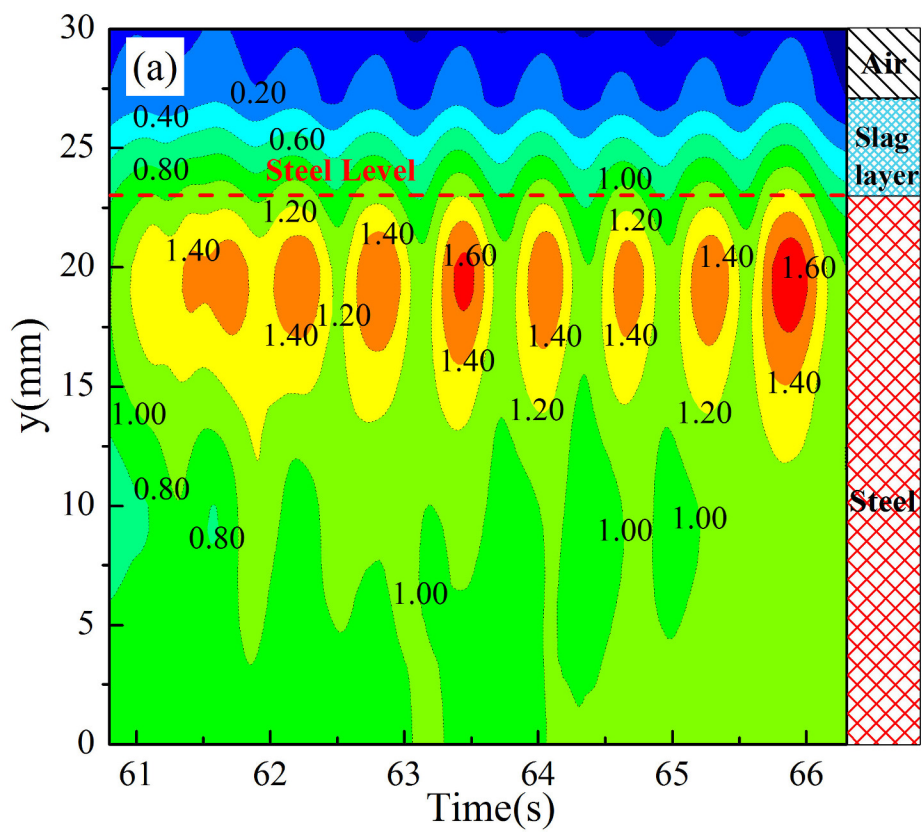


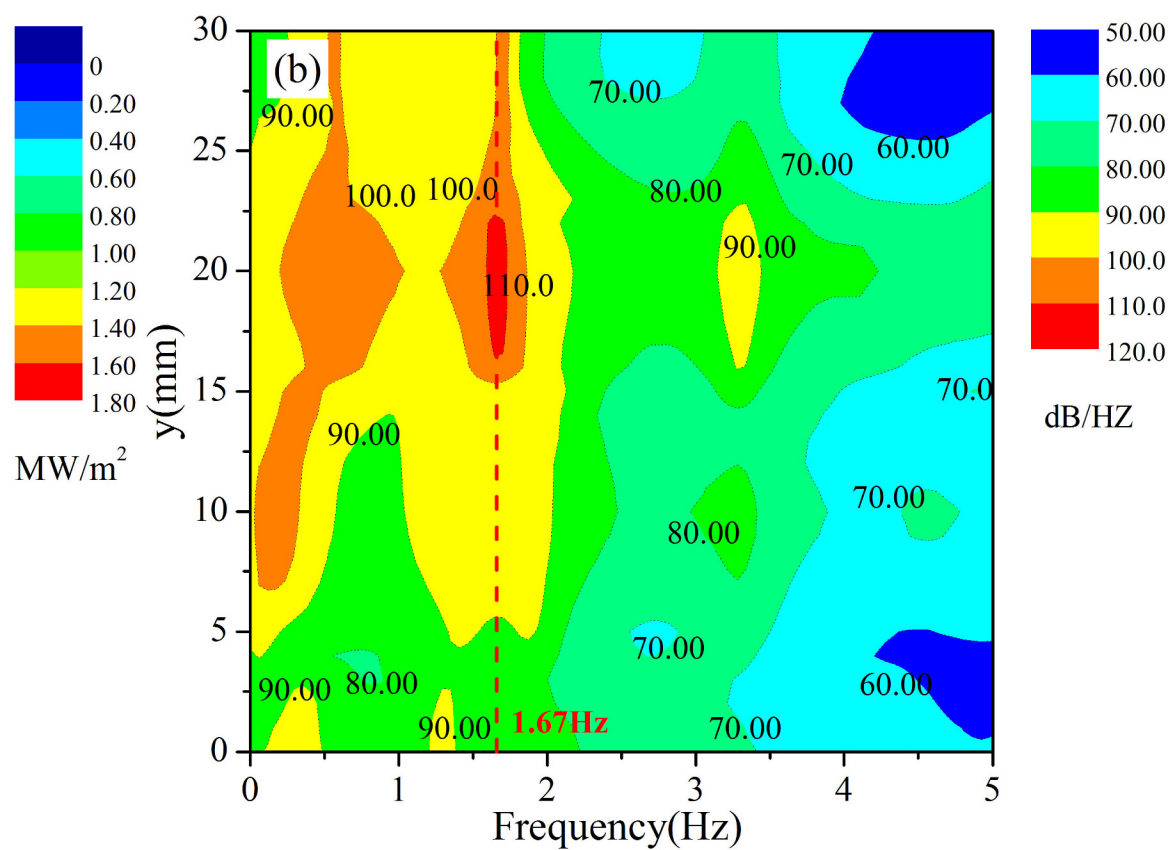
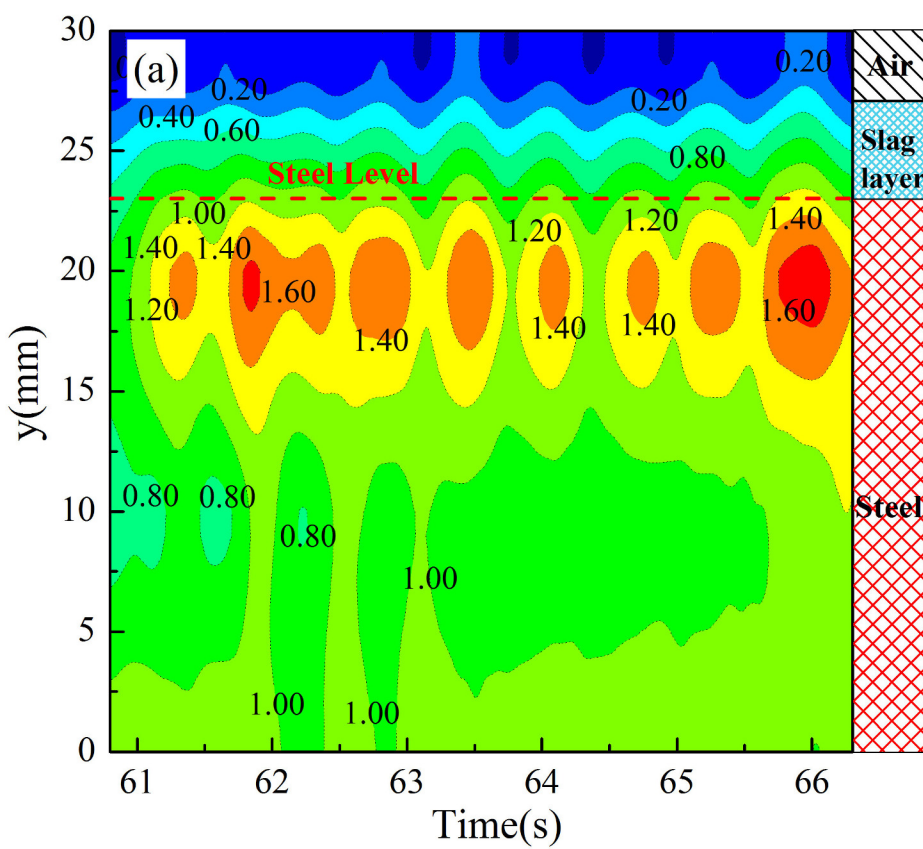
● Thermal couples(TC)

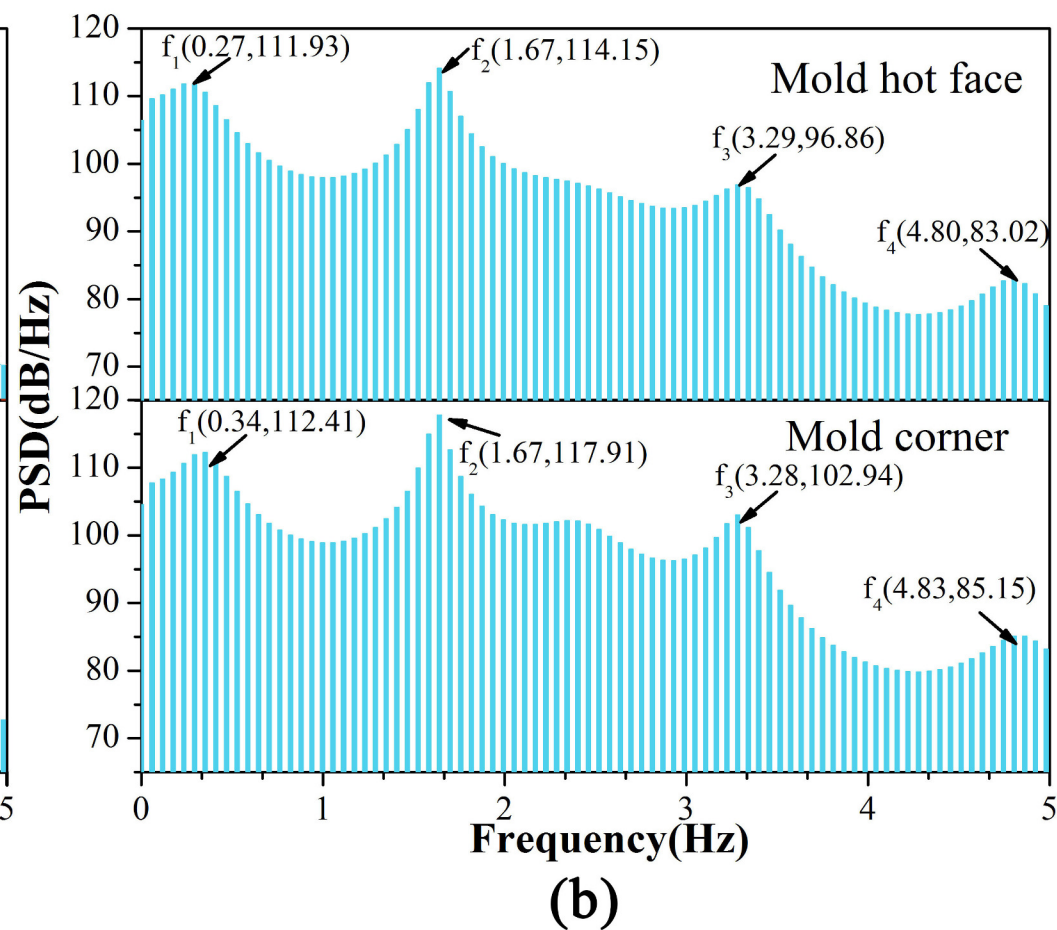
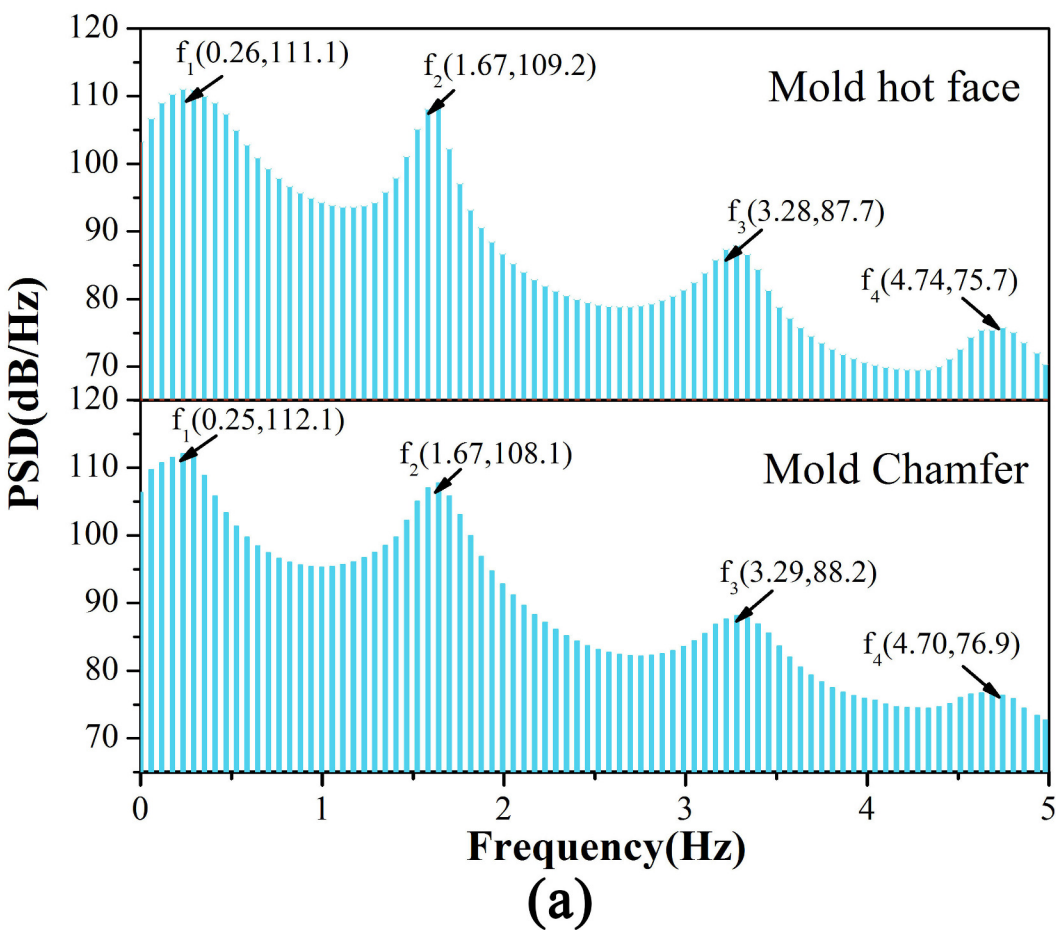
(b) Longitudinal section at mold chamfer

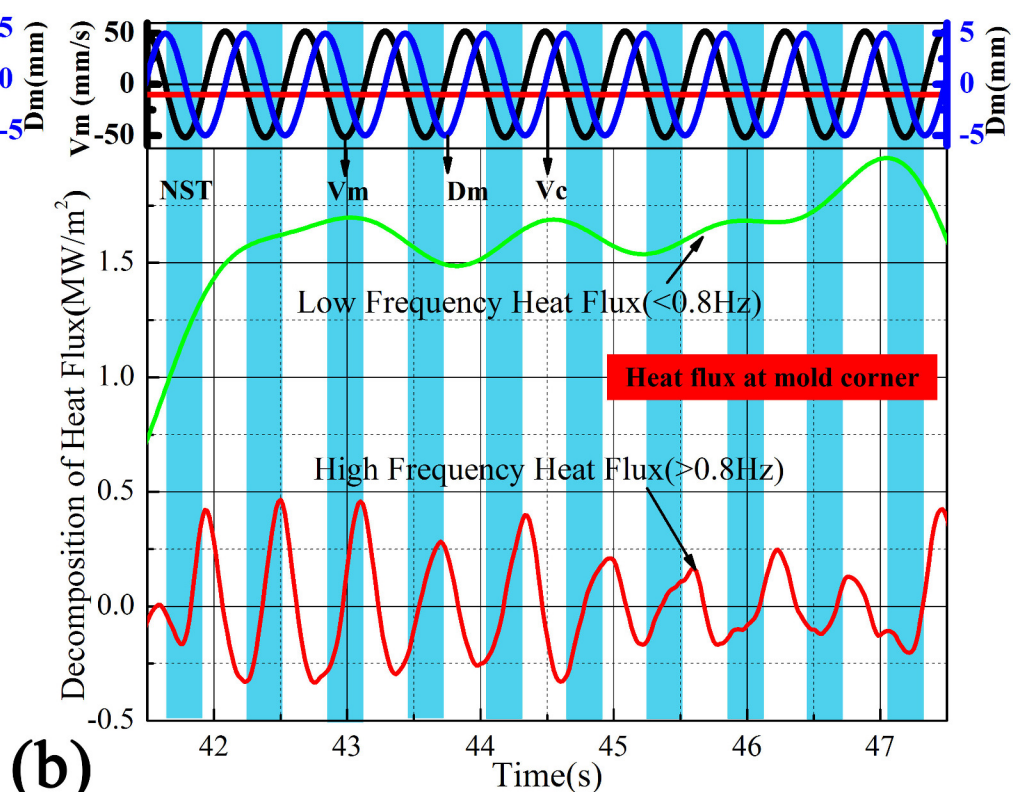
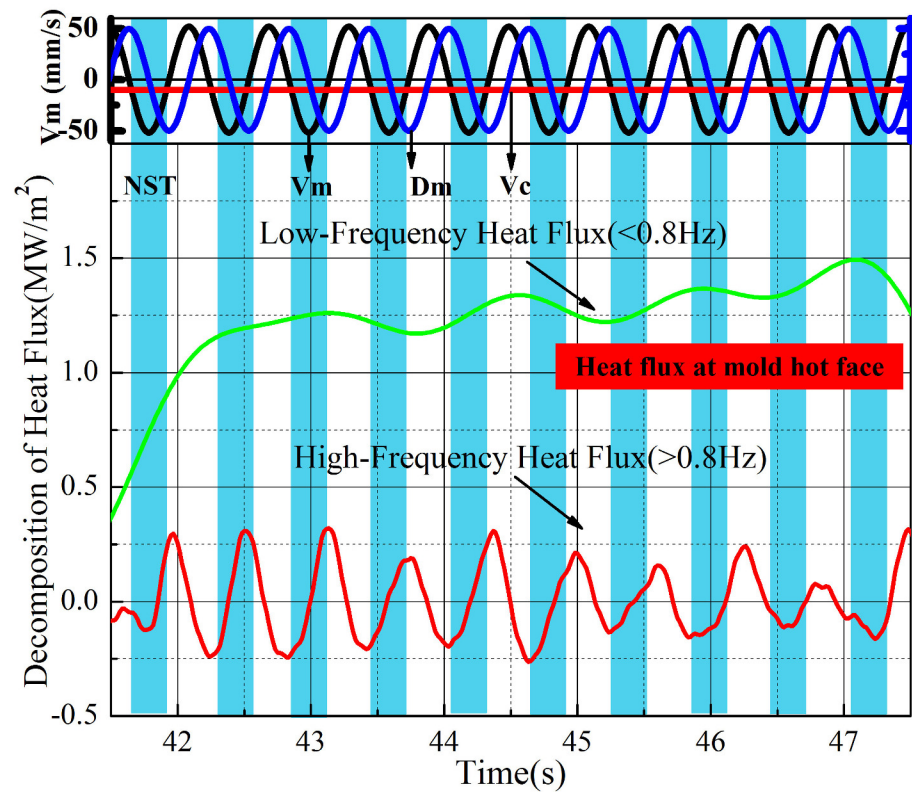
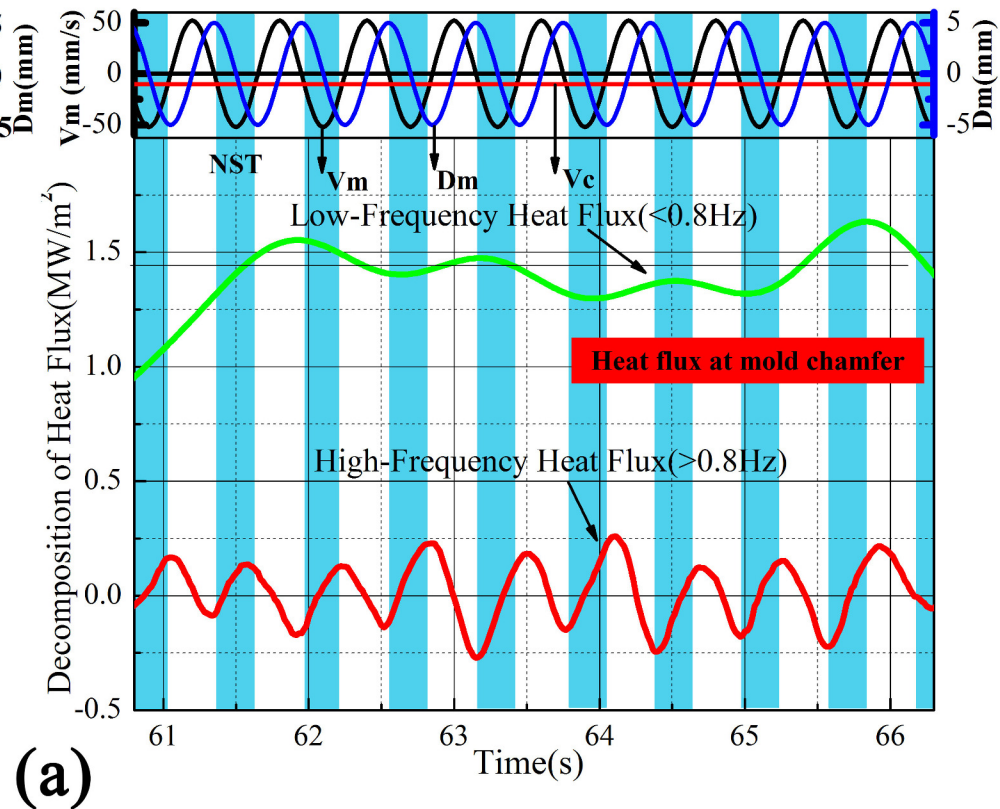
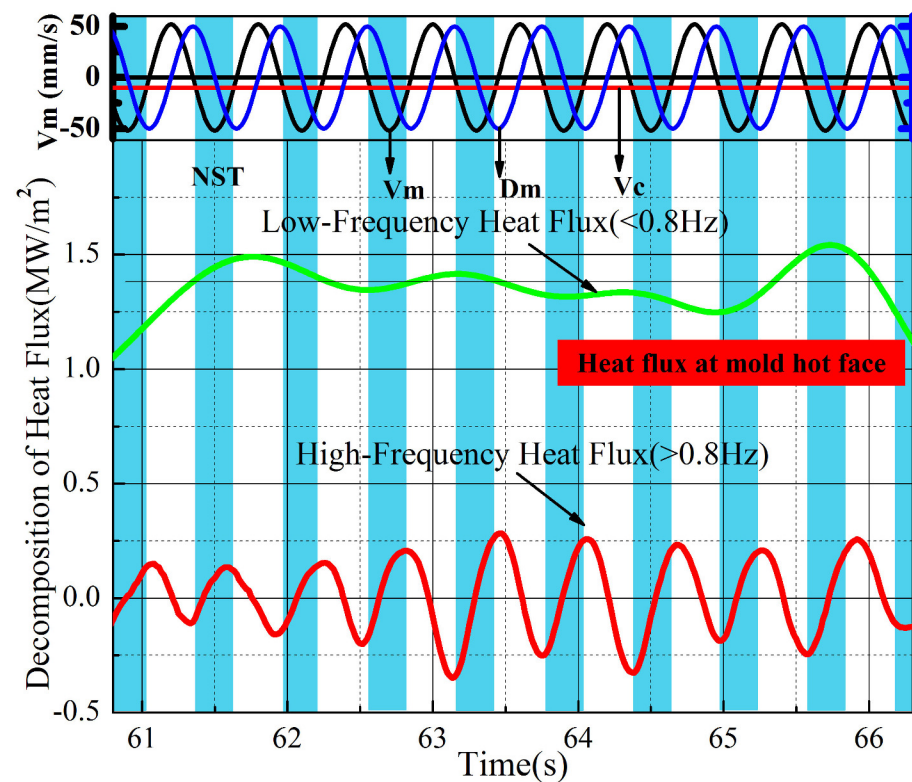


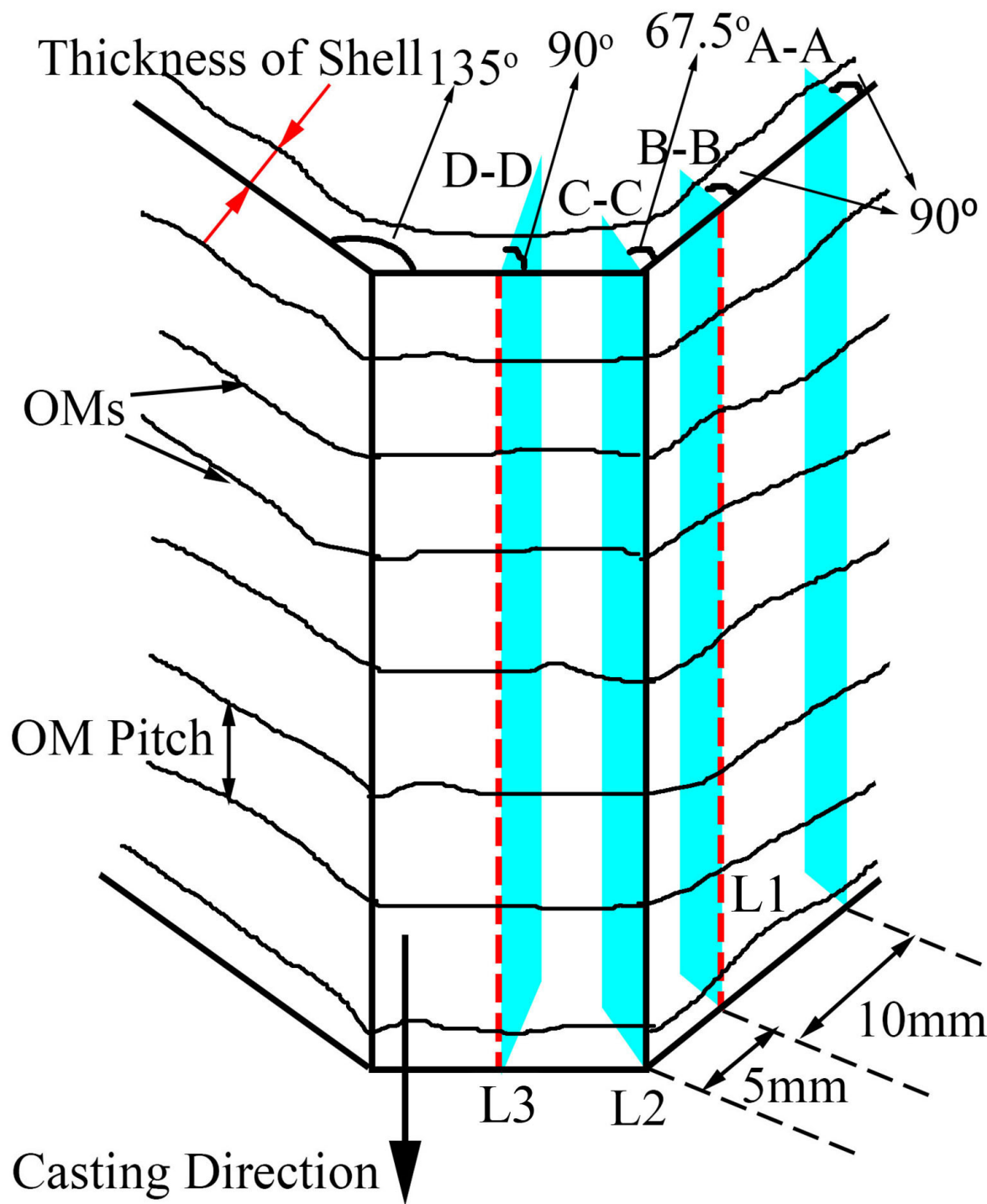
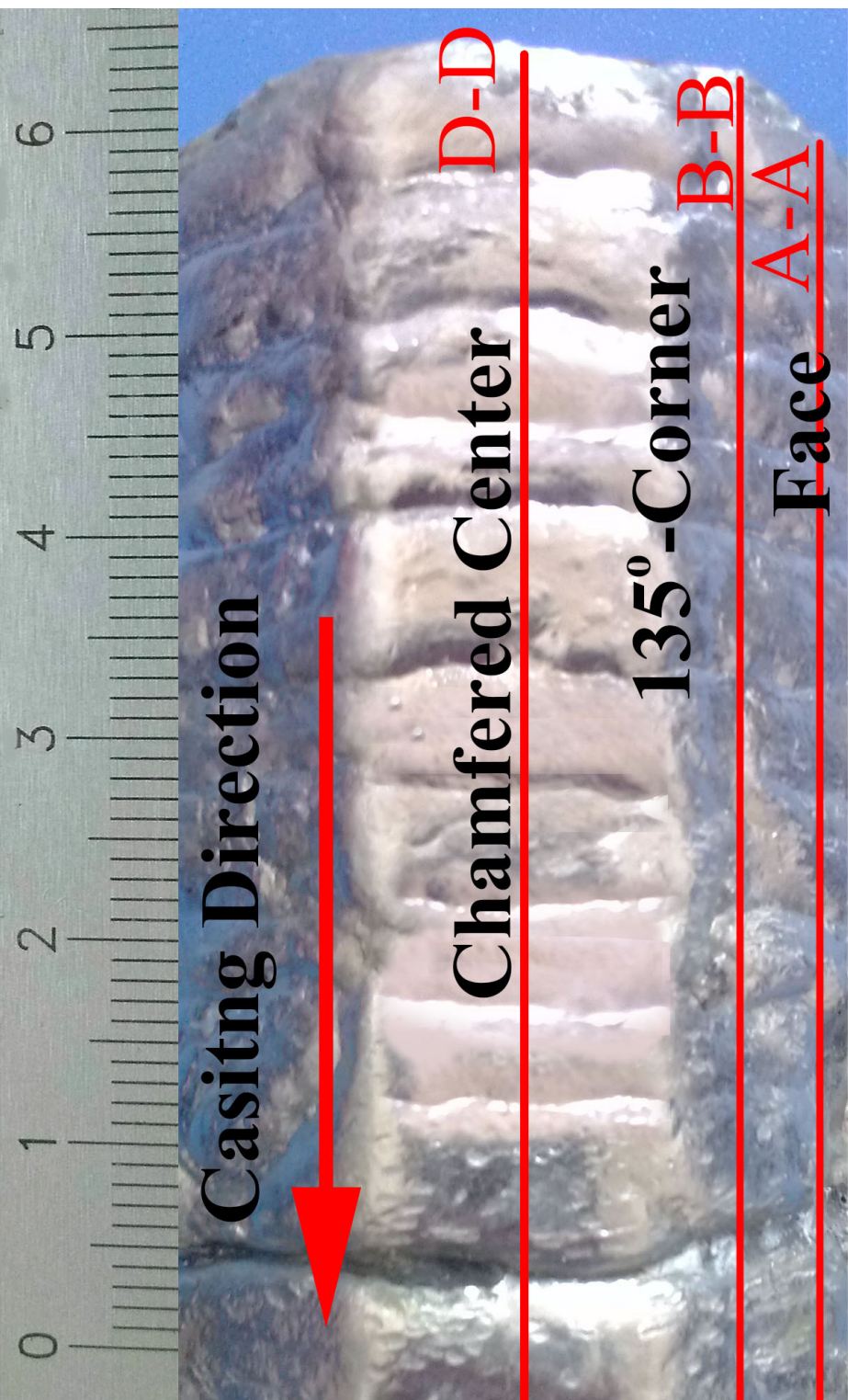


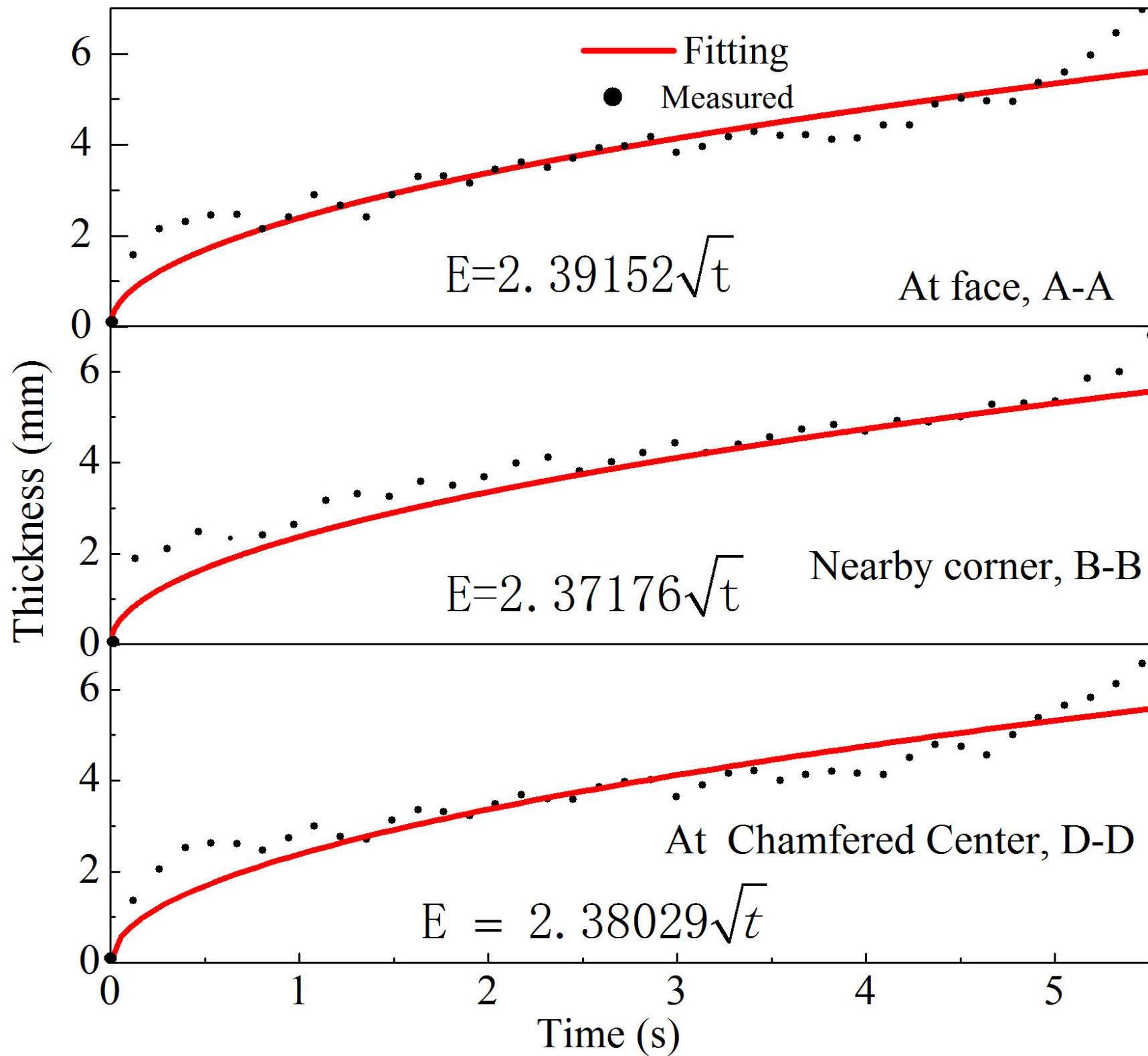


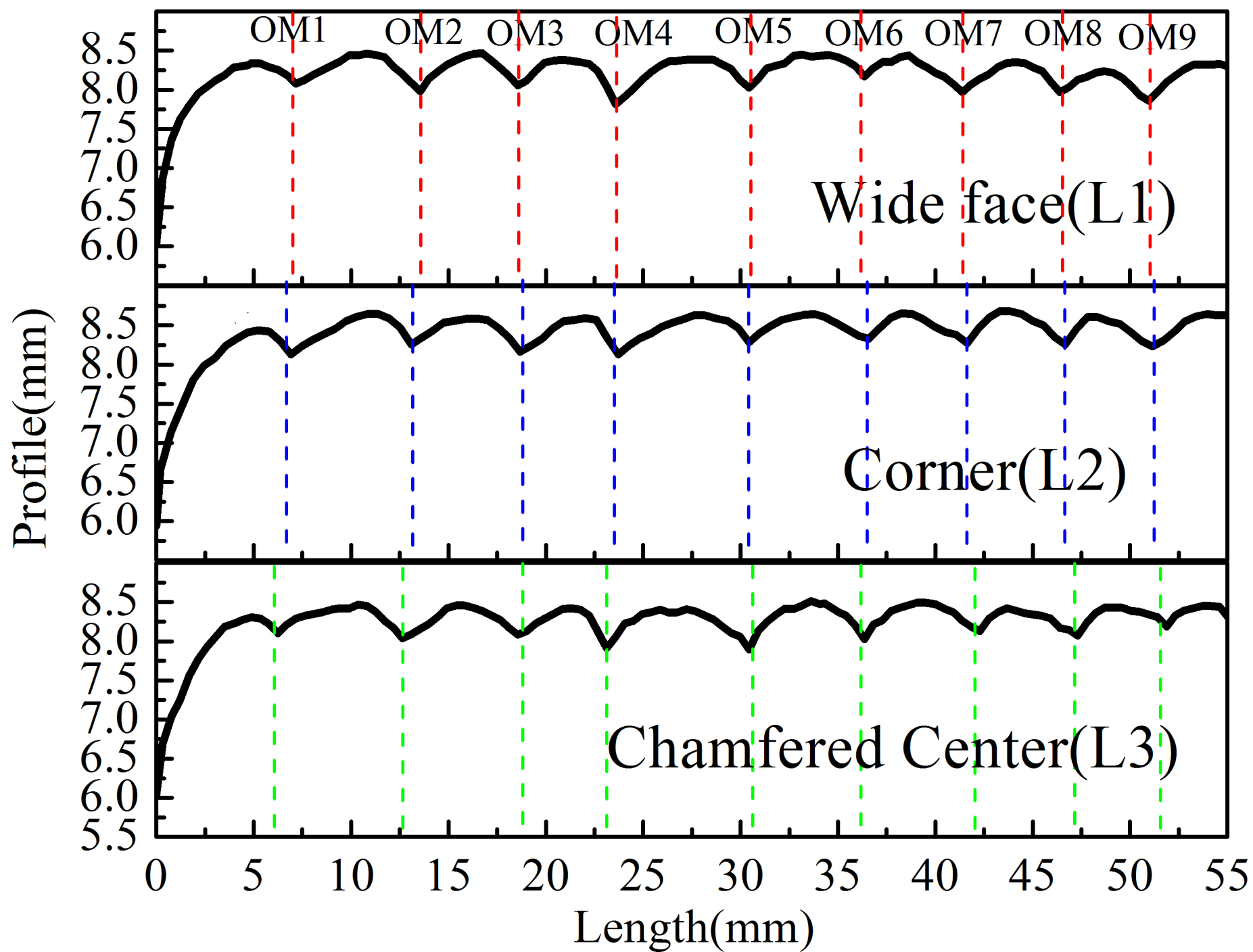




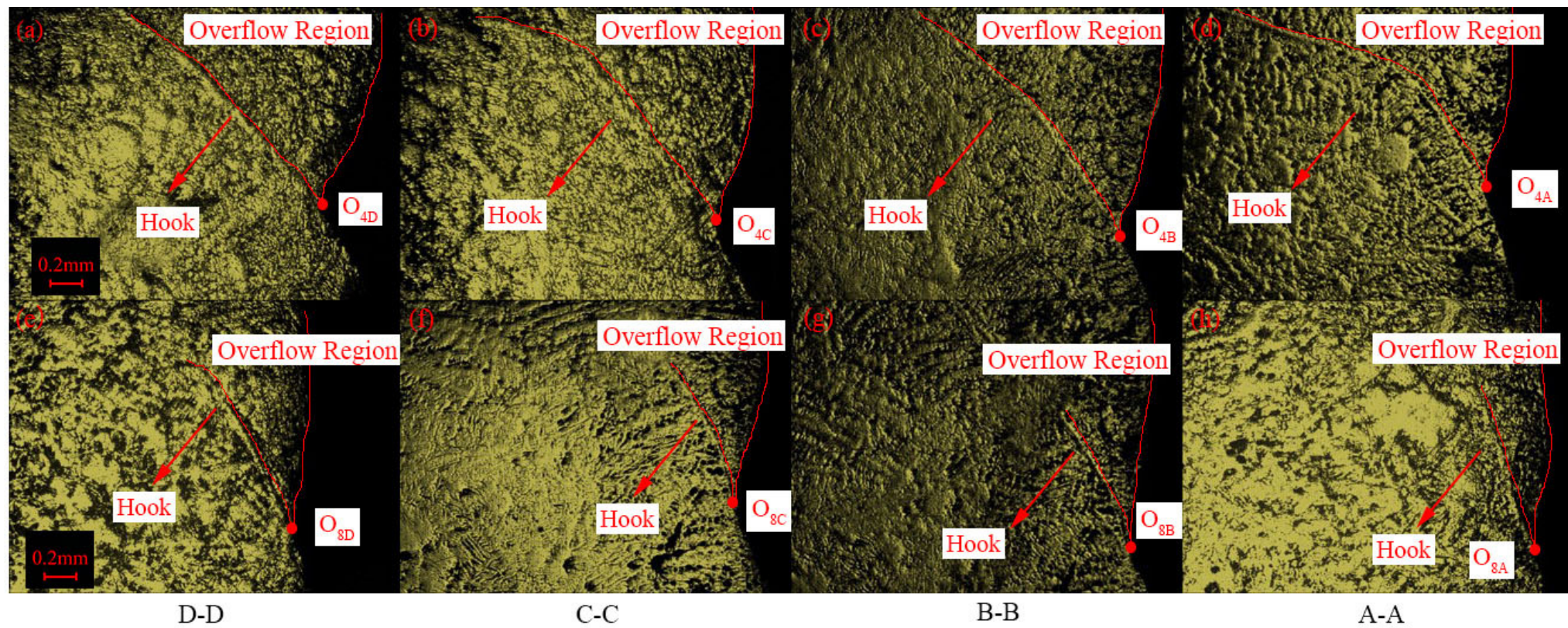








OM4



OM8

Table I. The Major Chemical Compositions of the Steel (Mass Percent %)

C	Si	Mn	P	S	Al	Ti	Nb
0.14	0.40	0.97	0.03	0.03	0.016	0.017	0.00047

Table II. The Major Chemical Compositions of the Mold Flux (Mass Percent %)

Basicity	CaO	SiO ₂	MgO	Al ₂ O ₃	Na ₂ O	B ₂ O ₃	Li ₂ O
1.15	41.72	36.28	2	4	8	6	2

Table III. Mold Oscillation Setting and Casting Conditions

Pouring Temperature[K(°C)]	Casting Speed(mm/s)	Frequency f (cpm)	Stroke(mm)	Temperature of Cooling Water[K(°C)]	NST(s)+PST(s)
1803(1530)	10	100(1.67Hz)	10	297(24)	0.26+0.34

Table IV. The Measured Pitch, Depth, and Height Difference for Each

Oscillation Mark at profile L1, L2 and L3

		OM1	OM2	OM3	OM4	OM5	OM6	OM7	OM8	OM9	Ave.	STD
Pitch (mm)	L1	—	6.58	5.13	4.91	6.91	5.65	5.22	5.13	4.60	5.52	0.77
	L2	—	6.45	5.70	4.66	6.95	6.07	5.13	5.02	4.60	5.57	0.81
	L3	—	6.57	6.18	4.39	7.43	5.55	5.96	5.03	4.36	5.68	1.00
Depth (mm)	L1	0.38	0.49	0.39	0.63	0.44	0.31	0.44	0.40	0.49	0.44	0.09
	L2	0.47	0.42	0.49	0.57	0.43	0.35	0.38	0.43	0.47	0.45	0.06
	L3	0.35	0.47	0.44	0.57	0.59	0.49	0.39	0.42	0.30	0.45	0.09
H_D (mm)	L1,L2	0.32	0.42	0.21	0.10	0.11	0.31	0.23	0.10	0.21	0.22	0.11
	L2,L3	0.62	0.61	0	0.42	0.21	0.31	0.42	0.5	0.32	0.38	0.19

*Where **Ave.** represents average value and **STD** represents standard deviation.

* H_D represents the height difference between two **OMs** roots of the same **OMs**.